AGU PUBLICATIONS

JGR

Journal of Geophysical Research: Oceans

RESEARCH ARTICLE

10.1002/2014JC010202

Key Points:

- Eddy-resolving model is used to simulate estimates of the SAMOC by XBT transect
- The errors associated with a reference level are the highest
- Satellite altimetry and XBT can be used to estimate the barotropic mode

Correspondence to:
M. Goes,
marlos.goes@noaa.gov

Citation:
Goes, M., G. Goni, and S. Dong (2015), An optimal XBT-based monitoring system for the South Atlantic meridional overturning circulation at 34°S, *J. Geophys. Res. Oceans*, *120*, doi:10.1002/2014JC010202.

Received 2 JUN 2014
Accepted 8 DEC 2014
Accepted article online 16 DEC 2014

An optimal XBT-based monitoring system for the South Atlantic meridional overturning circulation at 34°S

Marlos Goes[1,2], Gustavo Goni[2], and Shenfu Dong[1,2]

[1]CIMAS, University of Miami, Miami, Florida, USA, [2]PHOD, NOAA/AOML, Miami, Florida, USA

Abstract The South Atlantic is an important pathway for the interbasin exchanges of heat and freshwater with strong influence on the global meridional overturning stability and variability. Along the 34°S parallel, a quarterly, high-resolution XBT transect (AX18) samples the temperature structure in the upper ocean. The AX18 transect has been shown to be a useful component of a meridional overturning monitoring system of the region. However, a feasible, cost-effective design for an XBT-based system has not yet been developed. Here we use a high-resolution ocean assimilation product to simulate an XBT-based observational system across the South Atlantic. The sensitivity of the meridional heat transport, meridional overturning circulation, and geostrophic velocities to key observational and methodological assumptions is studied. Key assumptions taken into account are horizontal and temporal sampling of the transect, salinity, and deep temperature inference, as well as the level of reference for geostrophic velocities. With the current sampling strategy, the largest errors in the meridional overturning and heat transport estimations are the reference (barotropic) velocity and the western boundary resolution. We show how altimetry can be used along with hydrography to resolve the barotropic component of the flow. We use the results obtained by the state estimation under observational assumptions to make recommendations for potential improvements in the AX18 transect implementation.

1. Introduction

The Atlantic Ocean circulation exhibits a deep convection site at high latitudes in the Northern Hemisphere, which drives to a large extent the Atlantic meridional overturning circulation (AMOC) and, therefore, the meridional heat transport (MHT) toward the northern latitudes [*Marshall and Schott*, 1999]. The variability of the AMOC is partly responsible for changes in the Northern Hemisphere climate, such as the North Atlantic storm tracks [*Woollings et al.*, 2012] and the North American and European precipitation patterns [*Enfield et al.*, 2001; *Sutton and Hodson*, 2005], sea level variability [*Levermann et al.*, 2005; *Hu et al.*, 2011], uptake of ocean tracers such as CO_2 [*Sabine et al.*, 2004; *Goes et al.*, 2010], tropical precipitation [*Zhang and Delworth*, 2006], and El Niño patterns [*Dong and Sutton*, 2007; *Timmermann et al.*, 2007].

Despite the fact that the AMOC strength and variability are highly determined by changes within the North Atlantic Subpolar gyre [*Hatun et al.*, 2005; *Lohmann et al.*, 2009], the deep convection regions between the Greenland-Iceland-Scotland seas are highly sensitive to heat and freshwater transported from the South Atlantic [*Rahmstorf*, 1996; *Donners and Drijfhout*, 2004], which is suggested to be one of the main drivers of two stable states of the AMOC [*Weijer et al.*, 1999; *Beal et al.*, 2011; *Hawkings et al.*, 2011; *Garzoli et al.*, 2013].

The South Atlantic is an important pathway for exchange of heat and water masses from other basins through, for example, the Agulhas current region [*Goni et al.*, 1997] and the Brazil-Malvinas Confluence region [*Gordon*, 1986; *Wainer et al.*, 2000; *Goni and Wainer*, 2001; *Lentini et al.*, 2006; *Goni et al.*, 2011]. The South Atlantic Ocean has been historically one of the least observed regions on the globe; however, several efforts to measure long-term variability in the basin have been put forward in the last decade [*Dong et al.*, 2009; *Meinen et al.*, 2013; *Ansorge et al.*, 2014]. For instance, expendable bathythermograph (XBT) observations from the High-Density XBT transect AX18 (Figure 1a) obtain temperature sections in the upper 800 m of the ocean approximately 4 times a year along 34°S since 2002. Studies based on the AX18 XBT data have shown that the mean strength of AMOC and heat transport at 34°S are mostly geostrophically driven, although the seasonal variability of the meridional transports is equally determined by the geostrophic and the wind-driven Ekman components [*Dong et al.*, 2009]. The compensation between the Ekman and geostrophic components may translate into a small annual cycle of heat and volume transports [*Garzoli and*

 © 2014. American Geophysical Union. All Rights Reserved.

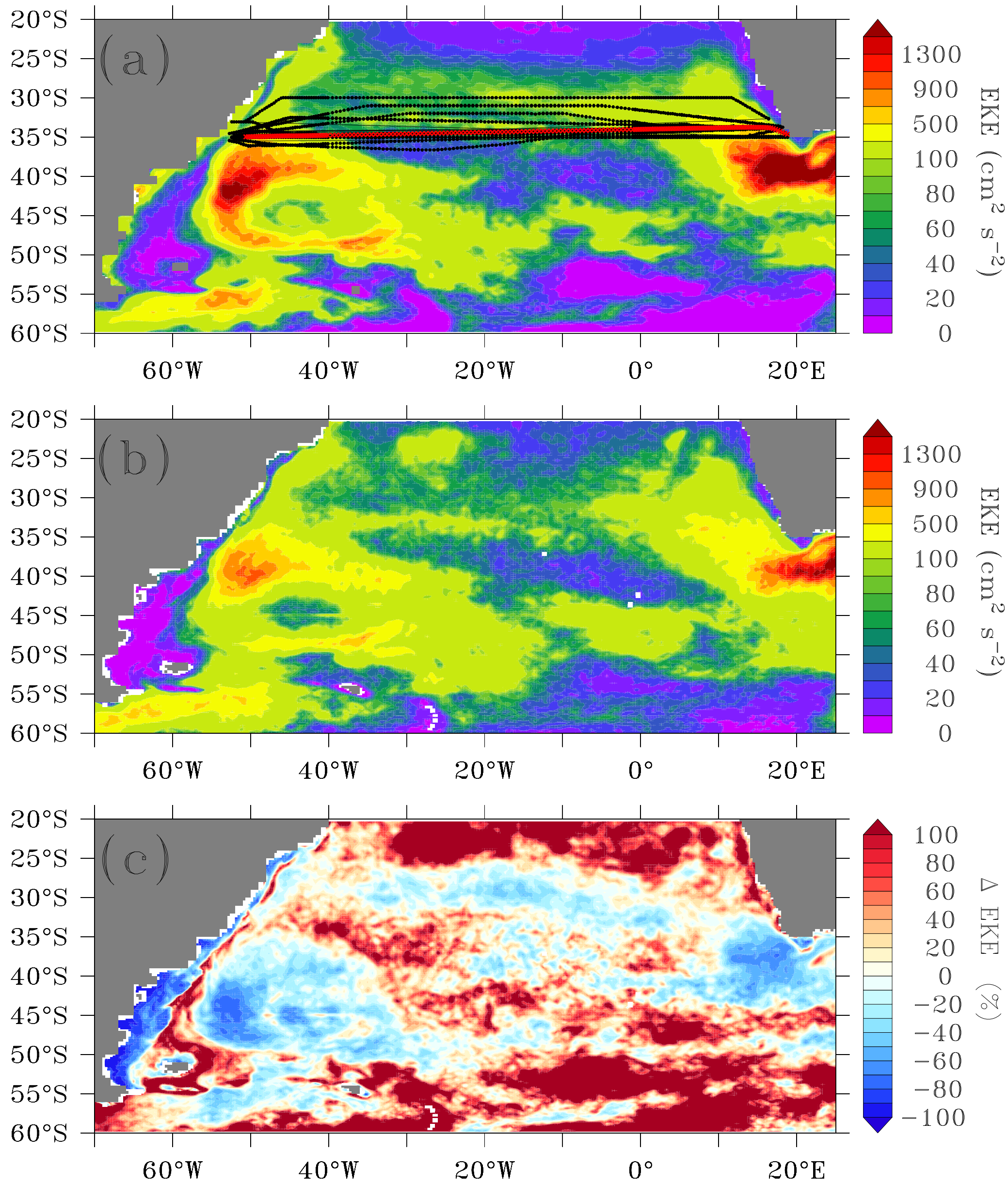

Figure 1. Eddy kinetic energy (cm^2 s^{-2}) derived from sea level anomalies for the period between 2007 and 2013, calculated using (a) AVISO observations, (b) HYCOM model, and (c) HYCOM minus observations (in percentage changes). The black lines in Figure 1a are the locations of the 18 selected AX18 realizations between 2002 and 2012, overlaid by a mean AX18 transect location in red.

Baringer, 2007; *Dong et al.*, 2009], although models generally do not reproduce this compensation characteristic of the observed annual cycle [*Dong et al.*, 2011a].

Currently, XBT-based estimates rely on several assumptions to estimate the integral flow in the South Atlantic. So far, only *Baringer and Garzoli* [2007] have estimated some of the uncertainty resulting from the underlying XBT-based observational system methodological assumptions to measure heat transport across 34°S. However, no sensitivity tests have yet been performed to derive an optimal AX18 sampling strategy, i.e., a feasible strategy that maximizes the information content in a cost-effective manner, and to assess the uncertainty in volume and heat transports associated with observational and computational methodologies across 34°S. To accomplish this, current high-resolution ocean reanalyzes can be useful to assess and investigate potential improvements in the sampling strategy of the AX18 transect. Similar methodologies have been applied, for example, in several studies in the North Atlantic [e.g., *Hirschi et al.*, 2003; *Baehr et al.*, 2004, 2008] to evaluate strategies for monitoring the AMOC in the North Atlantic.

 © 2014. American Geophysical Union. All Rights Reserved.

The goal of the present study is to assess how observational and computational methodologies affect the estimates of volume and heat transports across 34°S in Atlantic Ocean. We use a high-resolution model to help improve the design of the AX18 XBT transect in order to reduce uncertainty in its estimates. Therefore, this study will address four main objectives to reach these goals:

1. The optimal horizontal sampling along the AX18.
2. The optimal temporal sampling to capture the seasonal variability of the MOC and MHT in the region.
3. The uncertainties derived from the salinity and deep temperature estimation.
4. Potential improvements to the assumptions made regarding the level of reference to resolve the barotropic mode.

To address these objectives, we will first describe the characteristics of the region of study (section 2), and the high-resolution global assimilation model (section 3) used in this study. We will define the methodology (section 4) to calculate volume and meridional heat transport across 34°S, and perform controlled experiments in the model framework to answer point-by-point the above questions (section 5). Finally, we will discuss the results and make recommendations for the improvement of the AX18 XBT transect measurements (section 6).

2. Regional Characteristics

The subtropical South Atlantic is characterized by a large-scale anticyclonic feature, the South Atlantic subtropical gyre [*Stramma and England*, 1999; *Garzoli and Matano*, 2011]. In the southwestern Atlantic, the surface dynamics are dominated by the Brazil-Malvinas Confluence, which is characterized by the cold northward flow of the Malvinas Current, and a southward flowing warm weak western boundary current, the Brazil Current [*Garzoli*, 1993]. This region exhibits complex frontal motions [*Goni et al*., 2011; *Goni and Wainer*, 2001] and patterns with the simultaneous presence of warm and cold rings and eddies [*Lentini et al*., 2006] and, therefore, it is characterized by large values of eddy kinetic energy (Figure 1a). In the southeastern Atlantic, the transfer of warm waters from the Indian Ocean into the South Atlantic subtropical gyre largely takes place in the form of rings and filaments formed when the Agulhas Current retroflects south of Africa between 1°W and 25°E [*Richardson and Garzoli*, 2003; *Goni et al*., 1997]. The eastward flowing South Atlantic Current and the northward flowing Benguela Current delimit the southern and eastern boundaries of the subtropical gyre, respectively. The Brazil-Malvinas Confluence and the Agulhas retroflection regions represent the most energetic areas contained in the South Atlantic. These two regions present similar values of mean eddy kinetic energy, above 1000 $cm^2\ s^{-2}$ (Figure 1a), as revealed by altimetric sea level anomalies [*Ducet et al*., 2000] for the 2007–2012 time period. The Brazil-Malvinas Confluence and Agulhas retroflection regions are both crossed by the XBT transect AX18 (Figure 1a).

3. The HYCOM-NCODA Reanalysis

As suggested in previous studies, the strong mesoscale energy in the South Atlantic region requires a minimum of eddy-permitting models to resolve its main features [*Treguier et al*., 2007; *Biastoch et al*., 2009]. In the present study, we use data from the Hybrid Coordinate Ocean Model (HYCOM)-Navy Coupled Ocean Data Assimilation (NCODA) global assimilative product GLBa0.08 [*Chassignet et al*., 2009]. This product is chosen for its high resolution, and previous studies have shown that this model is appropriate for AMOC studies in the North Atlantic [e.g., *Xu et al*., 2014]. In addition, the data assimilation improves model performance in the South Atlantic [e.g., *Mello et al*., 2013]. We use a total of nearly 6 years of model simulation, from June 2007 to May 2013, sampled in a 7 day time step using 7 day averages.

The HYCOM-NCODA is configured for the global ocean with HYCOM 2.2 as the dynamical model. Computations are carried out on a Mercator grid between 78°S and 47°N, with an average of 1/12° (~7 km) horizontal resolution and 32 vertical layers. Bathymetry is derived from the U.S. Naval Research Laboratory 2 min DBDB2 (Digital Bathymetric Data Base) data set. Surface forcing is from the Navy Operational Global Atmospheric Prediction System (NOGAPS) and includes 3 hourly and 0.5° wind stress, wind speed, heat flux (using bulk formula), and precipitation. The NCODA methodology [*Cummings*, 2005] uses the model forecast as a first guess in a multivariate Optimal Interpolation (MVOI) scheme and assimilates available along-track satellite sea surface height anomaly observations (obtained via the Naval Oceanographic Office's Altimeter Data Fusion

© 2014. American Geophysical Union. All Rights Reserved.

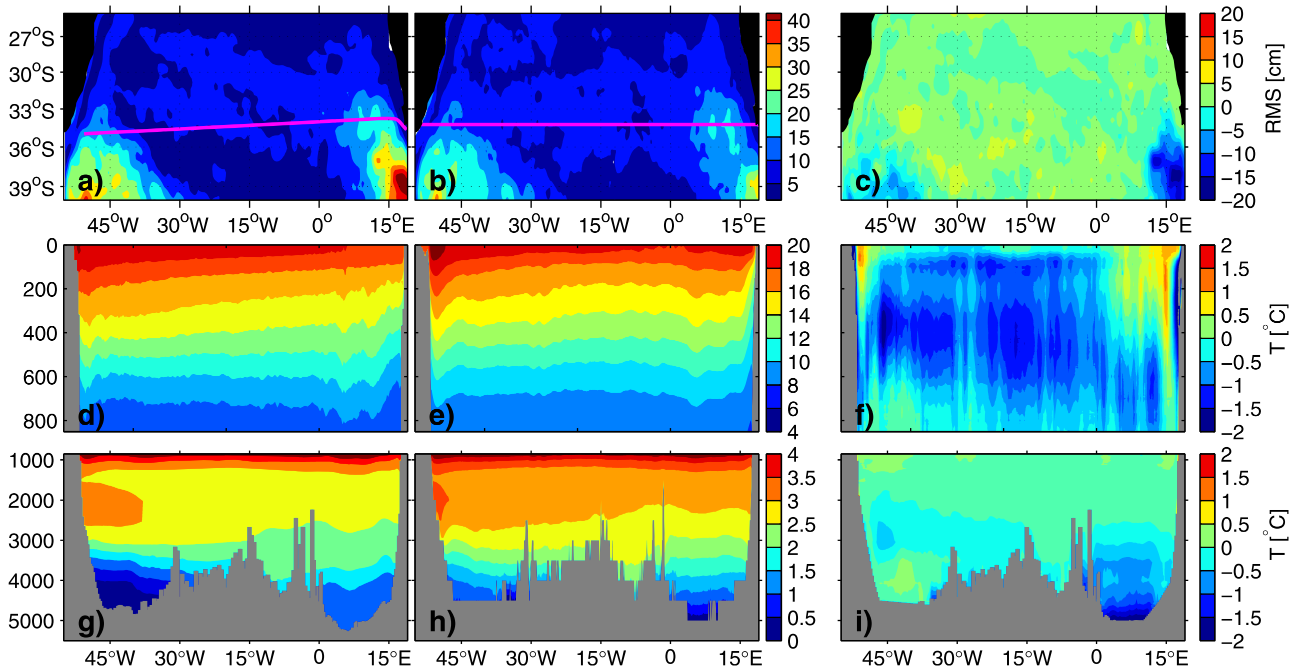

Figure 2. (a–c) Sea level anomaly (SLA) root-mean-square (RMS) contours (in cm) for: (a) AVISO overlaid with the mean AX18 transect (magenta line); (b) HYCOM overlaid with the model transect (magenta line); (c) HYCOM minus AVISO. Mean temperature sections contours (in °C) for: (d and g) observations, with AX18 data for the upper 850 m (Figure 2d) and WOA05 for 850 m to bottom (Figure 2g); (e and h) HYCOM model; (f and i) HYCOM minus observations.

Center), in situ sea surface temperature (SST), as well as available in situ vertical temperature and salinity profiles from XBTs, ARGO floats, and moored buoys. The Modular Ocean Data Assimilation System (MODAS) synthetic profiles are used by NCODA for downward projection of surface information [*Fox et al.*, 2002].

The eddy-resolving HYCOM reanalysis reproduces reasonably well the location and strength of the main circulation features of the South Atlantic as obtained from altimetric observations (Figure 1b). The output of this model, however, shows 40–60% lower energy in the high EKE regions, such as the Brazil-Malvinas Confluence and Agulhas retroflection regions, and up to 100% higher energy in the low EKE regions (Figure 1c). The root-mean-square (RMS) variability of sea level anomalies (SLA) also show up to 5 cm negative energy biases across the AX18 transect boundaries (Figures 2a–2c).

To compare the model thermohaline behavior with the actual XBT observations along the nominal 34°S, we select 18 realizations (Figure 2a) of the AX18 transect based on the criteria of being zonally directed (median angle $<10^\circ$, and with the mean latitude of the section between 30°S and 36°S). Below 850 m, the maximum depth sampled by the XBTs, the WOA05 annual climatology [*Locarnini et al.*, 2006] is used. The mean temperature section retrieved by the AX18 along the nominal of 34°S shows an east-west gradient, with higher upper ocean temperatures in the west (Figure 2d). The associated zonal density gradients allow average geostrophic volume and heat transports to the north, as shown in previous studies [e.g., *Ganachaud and Wunsch*, 2003; *Garzoli and Baringer*, 2007]. The model shows generally negative temperature biases in the interior (1–2°C on average), which indicates stronger stratification and shoaling of isothermal layers, and positive biases on the boundaries (1–1.5°C on average) relative to the mean AX18 section above 850 m, and stronger ocean bottom stratification in comparison to the WOA05 climatology (Figures 2g–2i).

4. Methodology

This study focuses on the reconstruction of the AMOC stream function (Ψ_y) and the meridional heat transport (MHT) along 34°S by simulating XBT observations in the model framework. For this, we use the temperature, salinity, and velocity outputs of the model, distributed over depth and longitude along 34.24°S, which is approximate location of the mean AX18 transect (Figure 2b). This section describes how the AMOC and MHT reconstructions are performed throughout the paper.

 © 2014. American Geophysical Union. All Rights Reserved.

4.1. AMOC

The AMOC stream function across a zonal section is defined as:

$$\Psi_y(z)=\int_{x_E}^{x_W}\int_{-H}^{z} v(x,z)dxdz, \tag{1}$$

i.e., the integral of the meridional velocity $v(x,z)$ from the bottom (H) to the depth (z) of the ocean and between the western (x_W) and the eastern (x_E) boundaries of the basin. In order to reconstruct the AMOC stream function using simulated ocean observations, the estimated meridional velocity $\tilde{v}$ (x,z) is defined as the sum of three dynamical components [*Lee and Marotzke*, 1998]:

$$v(x,z)\simeq\tilde{v}(x,y)=v_{sh}(x,z)+v_E(x,z)+v_{bar}(x), \tag{2}$$

namely the vertical shear (v_{sh}), Ekman (v_E), and barotropic (v_{bar}) components, respectively. To calculate v_{sh}, first the geostrophic velocity (v_g) is estimated. v_g is calculated using the thermal wind relationship, in which zonal gradients of density ($\rho(x,z)$) define the vertical shear relative to a chosen reference level (z_{ref}) where a reference velocity (v_{ref}) may be specified:

$$v_g(x,z)=-\frac{g}{\rho_0 f}\int_{z_{ref}}^{z}\frac{\partial\rho(x,z)}{\partial x}dz+v_{ref}(x), \tag{3}$$

where $\rho_0=1025$ kg m^{-3} is the mean water density, f is the Coriolis parameter, and g is the local gravity. The density gradients in v_g are calculated similarly to *Baehr et al*. [2004], but using a centered differences method. From (3), we specify v_{sh} as the geostrophic velocity subtracted locally by its depth average ($\bar{v}_g$) [*Hirschi and Marotzke*, 2007]:

$$v_{sh}(x,z)=v_g(x,z)-\bar{v}_g(x). \tag{4}$$

The velocity v_{sh} is then subtracted by a spatially constant term proportional to the weighted mean velocity across the section to ensure zero mass transport across the section [*Baehr et al*., 2004; *Hirschi et al*., 2003].

The second term in (2) is the Ekman velocity component $v_E(x,z)$, calculated according to *Baehr et al*. [2004]. The Ekman velocity is derived from the zonal integral of the zonal wind stress (τ_x), divided by the area of the zonal transect above the depth of the Ekman layer (D_E), arbitrarily assumed to be $D_E=50$ m [e.g., *Pond and Pickard*, 1983]. $v_E(x,z)$ is then compensated by a depth-uniform return flow [*Jayne and Marotzke*, 2001], and further subtracted by its vertical average ($\bar{v}_E$), which is incorporated in the external mode. Other small ageostrophic contributions rather than Ekman (e.g., frictional and nonlinear) are not defined, but may be included in the vertical shear component [*Lee and Marotzke*, 1998]. The barotropic or gyre component (last term in (2)) is depth independent, and contains the vertically averaged information of the meridional velocity, which constitutes the external mode [*Hirschi and Marotzke*, 2007]. The barotropic velocities are reconstructed by the sum of the vertical average terms of the geostrophic and Ekman components:

$$v_{bar}(x)\simeq\frac{1}{H}\int_{-H}^{0}\tilde{v}(x,z)dz=\bar{v}_g+\bar{v}_E, \tag{5}$$

and also corrected by a spatially constant term to ensure zero mass transport. The barotropic component has a strong contribution to the geostrophic flow at locations of sloping bottom topography and near the boundaries where frictional effects are important. At these regions, the external mode component has an important projection on the AMOC reconstruction [*Baehr et al*., 2004].

The AMOC strength (in Sv) is further defined as the value of the maximum amplitude of the AMOC stream function in (1). Since the total velocity is decomposed into its physical components in (2), an AMOC strength can be similarly defined for the individual components of the AMOC.

4.2. Meridional Heat Transport

The meridional heat transport is calculated as follows:

$$MHT=\rho_0 c_p\int_{-H}^{0}\int_{x_E}^{x_W} v(x,z)\theta(x,z)\,dxdz-\rho_0 c_p M_y\langle\theta\rangle, \tag{6}$$

where $c_p=4187$ J kg^{-1}K^{-1} is the specific heat of sea water, M_y is the volume transport across the section, and $\langle\theta\rangle$ is the averaged potential temperature θ along the section. The last term in (6) is a constraint to

©2014. American Geophysical Union. All Rights Reserved.

allow zero mass transport across the section, which is necessary for heat transport calculations using the original model velocities in free surface models, since they do not necessarily have zero mass transport at any given time period [*Jayne and Marotzke*, 2001; *Griffies et al.*, 2004]. Otherwise, the calculated heat transport would be dependent on an arbitrary temperature reference [*Montgomery*, 1974].

To reconstruct the MHT, equation (6) is further decomposed into the same components as the meridional overturning, i.e., vertical shear, Ekman, and barotropic, respectively, using the corresponding decomposition of the velocity (2). Following *Hall and Bryden* [1982]:

$$MHT \simeq \rho_0 c_p \int_{-H}^{0} \int_{x_E}^{x_W} \{ v_{vs}[\theta - \theta_{bar}] + v_{Ek}\theta_{Ek} + v_{bar}\theta_{bar} \} dxdz, \tag{7}$$

where θ_{bar} is the depth-averaged potential temperature, and θ_{ek} follows the Ekman velocity definition, i.e., θ_{ek} assumes only two values over the section, one as the average θ in the Ekman layer, and another in the layer below the Ekman layer. All the velocity components in (7) are designed to be compensated to allow zero net volume transport across the section. Therefore, the constraint used in (6) can be dropped in the reconstruction, and still each of the terms in (7) is meaningful as a heat transport [*Hirschi et al.*, 2003].

5. Results

5.1. AMOC Stream Function and MHT Reconstructions: A Perfect Model Approach

In this section, we evaluate the methodology described in section 4 for the reconstructions of the AMOC and MHT in the model, and define a ground truth for a later comparison with the AMOC and MHT reconstructions using the approximations of an XBT observing system. To do this, we perform a "perfect" model decomposition, in which we assume perfect observations (i.e., error free and full model spatial and temporal coverage), in that no observational approximations rather than the ones used to calculate the dynamical components themselves are used. Therefore, the reconstructed absolute geostrophic velocities (equation (3)) are calculated at every time step using a level of known motion near the bottom of the ocean, assuming that reference velocities are perfectly known. We use full-depth information at all model grid points to calculate the density gradients in the vertical shear component. The Ekman component is computed using the model zonal wind stress at all model grid points and locations. The AMOC strength calculated directly from the model velocities is highly variable in time (Figure 3a; black line), with amplitudes ranging from -5 to 35 Sv (1 Sv $=10^6$ m^3 s^{-1}), and with strong high frequency variability as well as a defined annual cycle. The time-averaged AMOC stream function (Figure 3c) shows positive (northward) values in the upper 3700 m, negative (southward) values underneath, and a pronounced maximum at the depth of $\sim$1500 m, which characterizes the AMOC strength. The time-mean AMOC strength in the model is 15.1 $\pm$ 6.8 Sv, lower than observational estimates of 17.9 $\pm$ 2.2 Sv [*Dong et al.*, 2009], but within the uncertainty estimates. Results from other high-resolution models [e.g., *Dong et al.*, 2011a] show a strong agreement with the AMOC strength value (15.0 $\pm$ 3.7 Sv) presented here.

We decompose the AMOC stream function into its vertical shear, Ekman, and barotropic components using the methodology described in section 4.1. Individually, the vertical shear component has the strongest contribution to the mean AMOC strength (Figure 3b), with an average of 26.9 $\pm$ 3.6 Sv, and it is in great part compensated by the barotropic contribution of the transport, which is negative (southward) with an average of -16.3 ± 6.3 Sv. The resulting absolute geostrophic transport is 12.6 $\pm$ 3.2 Sv, smaller than the observational value of 15.7 $\pm$ 2.6 Sv [*Dong et al.*, 2009], but similar to that obtained from the OFES model (12.9 $\pm$ 2.1 Sv) [*Dong et al.*, 2011a]. It is worth mentioning that neither the barotropic nor the vertical shear stream functions show a reversal in depth, as observed on the total mean stream function, but that the addition of these two stream functions produces the same reversal pattern at approximately 3700 m (magenta line in Figure 3c) as observed in the original model stream function. Strong interannual variability is observed in the barotropic component, with positive anomalies in the austral summer of 2007 and 2008 and negative anomalies in the austral spring of 2009 and 2010. Recent studies using the same model and direct AMOC observations from the RAPID array [*McCarthy et al.*, 2012; *Xu et al.*, 2014] found similar AMOC variability in the 2008 and 2009/2010 periods, and attributed the anomalies in the 2009/2010 period to a low North Atlantic Oscillation (NAO) phase. In addition, *Boening et al.* [2011] found a strong ocean bottom pressure anomaly in late 2009 in the South Pacific attributed to a strong wind stress curl anomaly in the

© 2014. American Geophysical Union. All Rights Reserved.

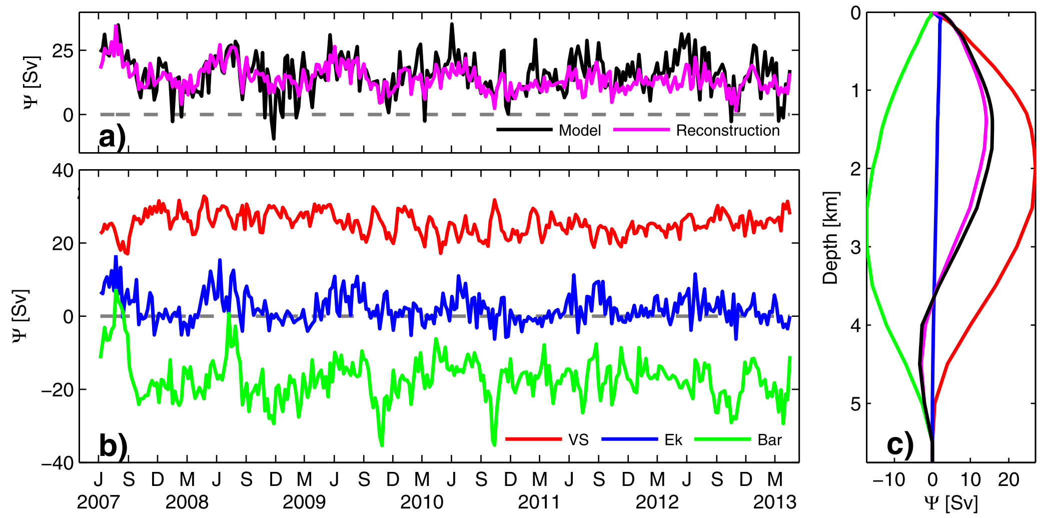

Figure 3. (a) Maximum volume transport stream function (AMOC) using model velocities (black) and the reconstruction (magenta). (b) AMOC decomposition into vertical shear (red), Ekman (blue), and barotropic (green) components. (c) Time-mean meridional transport stream function for the model velocities (black), reconstruction (magenta), Ekman (blue), vertical shear (red), and barotropic (green). The level of reference is assumed to be on the ocean bottom using the model bottom velocities as the reference.

region. Whether the 2009/2010 variability observed at 34°S is caused by similar mechanisms is still to be ruled out. The Ekman component has the lowest contribution to the mean AMOC strength, only 2.0 ± 4.0 Sv, but its maximum amplitude of variability can reach over 10 Sv, which is stronger than the other components.

The MHT follows the same pattern as the AMOC (Figure 4). The mean MHT calculated directly from the model fields is 0.33 ± 0.5 PW (1 PetaWatt $=10^{15}$ W), which is also lower than the values calculated from observational studies (0.54 ± 0.14 PW) [*Garzoli et al.*, 2013]. In the MHT reconstruction, the barotropic MHT component (−0.60 ± 0.23 PW) compensates to a large extent the vertical shear component (0.81 ± 0.15 PW), and the Ekman component contributes about one third of the total MHT (0.12 ± 0.24 PW).

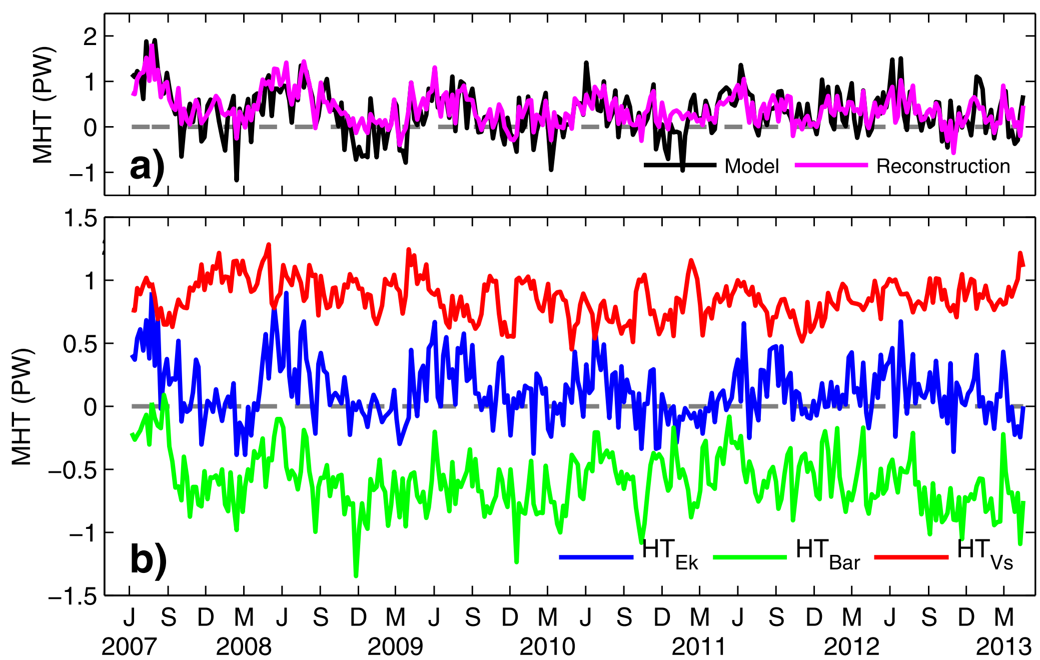

Figure 4. (a) Meridional heat transport (MHT in PW) using model velocities (black) and reconstruction (magenta). (b) MHT decomposition into vertical shear (red), Ekman (blue), and barotropic (green) components. The level of reference is assumed to be on the ocean bottom using the model bottom velocities as the reference.

© 2014. American Geophysical Union. All Rights Reserved.

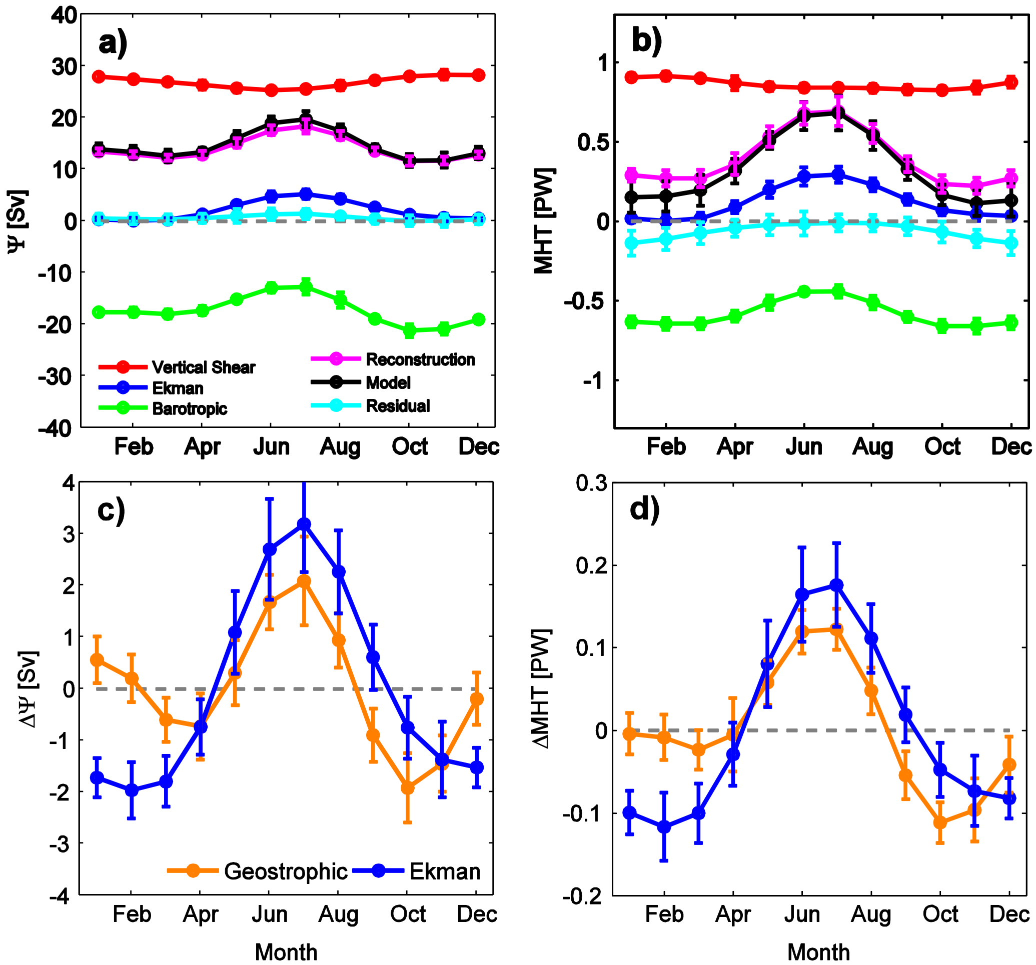

Figure 5. Seasonal variability constructed as the sum of annual and semiannual harmonics of the (a) AMOC and (b) MHT components time series: vertical shear (red), Ekman (blue), and barotropic (green). The reconstruction (magenta) is the sum of the transport components, which is comparable to the total transport from the original model velocities (black). (c and d) The AMOC and MHT residuals relative to the annual mean for Ekman and geostrophic components. The level of reference is assumed to be on the ocean bottom using the model bottom velocities as the reference.

The annual variability of the reconstructed AMOC and MHT components is calculated as the sum of the first and second harmonics of the reconstructed time series (Figure 5). The vertical shear component does not have a significant annual cycle, although lower transport values are found during the austral winter. By doing similar analysis as in *Dong et al*. [2014], we find that the reduced seasonal cycle of the vertical shear component may be a result of an out-of-phase relationship of density anomalies within the mixed layer (50 m) and below it, in both western and eastern boundaries. The Ekman and barotropic components have stronger annual cycles (Figures 5a and 5b), and are approximately in phase with each other, with more positive/less negative values from March to August. Therefore, the reconstructed geostrophic and the Ekman components have similar amplitudes and phases (Figures 5c and 5d), a result that differs from previous observational studies [e.g., *Dong et al*., 2009] in that there is an out-of-phase relationship between the Ekman and geostrophic components of the AMOC annual cycle, which produces a much reduced annual cycle of the AMOC variability. However, other high-resolution models also show a similar annual cycle for the total AMOC [e.g., *Dong et al*., 2011a; *Perez et al*., 2011] as observed here.

As observed in Figures 3a and 4a, the model AMOC and MHT shows strong high frequency variability and occasionally negative values during austral summer, particularly for the MHT. These reversals of the model transport are hardly featured in their reconstructions. The residual contribution, which is the part of the annual variance that is not explained by the reconstruction (cyan line, Figure 5), can reach 3.3 Sv in the austral winter for the AMOC and up to −0.2 PW for the MHT during the austral summer.

 © 2014. American Geophysical Union. All Rights Reserved.

Consequently, the reconstruction produces a lower mean (14.1 $\pm$ 4.9 Sv) for the AMOC and a higher mean (0.39 $\pm$ 0.36 PW) for MHT. These differences may arise because the model velocities contain frictional and ageostrophic terms other than Ekman [*Sime et al*., 2006]. Therefore, we define the ageostrophic eddy variability in the model as the AMOC strength residual between the model and the reconstruction, and estimate this contribution to be 0.6 $\pm$ 5.0 Sv and $-$0.06 $\pm$ 0.32 PW. Additional residual contributions can come from the unbalanced flow of volume (0.94 $\pm$ 3.8 Sv), whose MHT contribution is here estimated at $-$0.02 $\pm$ 0.06 PW (equation (7)), the same mean magnitude of 0.02 PW estimated in *Baringer and Garzoli* [2007].

5.2. XBT Observational Strategy

The AX18 XBT transect, which was designed with the main purpose of monitoring the variability of the upper limb of the AMOC transport, measures temperature sections in the upper ocean between Cape Town and South America quarterly, with a high-density (between 25 and 50 km) zonal spacing.

Observational studies that used AX18 data to estimate meridional volume and heat transports involved several methodological assumptions. The XBTs measure temperature profiles in the upper 800 m depth (e.g., Deep Blue probe type). Because XBTs do not measure salinity, a common method to infer salinity profiles at an XBT deployment location uses a lookup table derived from historical temperature-salinity (T-S) relationships [*Thacker*, 2008]. Below 800 m, the temperature and salinity profiles are extended down to the bottom of the ocean with their climatological values [*Baringer and Garzoli*, 2007; *Dong et al*., 2009]. The barotropic or external mode is generally estimated by adopting a level of no motion at the depth where the potential density anomaly referenced to 2000 dbar assumes the value of 37.09 kg m^{-3} (σ_2=37.09) [*Ganachaud and Wunsch*, 2003; *Baringer and Garzoli*, 2007]. The σ_2=37.09 depth is approximately located at a depth of 3700 m and between two water masses, the North Atlantic Deep Water (NADW) flowing southward between 1500 and 3700 m, and the underlying Antarctic Bottom Water (AABW) flowing northward [*Ganachaud and Wunsch*, 2003]. The Ekman component of the flow is calculated from available zonal wind stress products at the XBT deployment locations.

In order to simulate the XBT observations in the model, we make the same assumptions as used in the observational studies: (i) the model temperature data are used above 800 m, (ii) a quadratic least squares fit between the annual mean temperature and salinity obtained from the model is specified for each depth, calculated using 1° boxes along 34°S, (iii) the monthly climatology of temperature and salinity at a 1° longitudinal resolution is padded below 800 m to extend the pseudoobservations to the bottom of the ocean, and (iv) a reference level for the geostrophic velocity calculation is chosen. Constructing the T-S relationships from the model instead of using, for example, the World Ocean Atlas (WOA) climatology is necessary, since the model's own internal biases relative to the observations could potentially bring spurious T-S discontinuities. The WOA climatology is subject to biases in regional coverage, such as below 2000 m (the parking depth of Argo floats), along coastal areas, and historically in the South Atlantic. Here we do not account for imperfect sampling although its effects can be sizeable in producing additional seasonal biases.

The RMS error between the model salinity and the salinity estimated from the lookup table is shown in Figure 6. In the top 200 m, salinity errors are on the order of 0.1 psu. Higher differences ($\sim$0.4 psu) are found in the western side of the basin in the upper 100 m, where there is a freshwater inflow from river runoff. Below 200 m, the RMS difference is generally lower than 0.1 psu, with higher values located around 500 m and decreasing to near zero below 1000 m. These error values are on the same order of magnitude of the RMS of the salinity annual cycle and, therefore, are highly driven by the seasonal variation of T-S relationships, which is not captured by the annual mean T-S relationships.

5.3. AMOC and MHT Uncertainties Due to the XBT Transect Observational Sampling

In this section, we investigate the meridional transport uncertainties associated with the observational sampling. We will explore two main sources of uncertainty, that relate to: (i) the temporal resolution and (ii) the horizontal resolution. We apply each of the two assumptions individually in order to quantify their uncertainties, which will allow recommending improvements in the AX18 transect design and implementation.

5.3.1. Temporal Resolution

The AX18 transect was originally implemented to be carried out 4 times a year, and AMOC estimates can only be performed at the time of each AX18 transect realization. The rate of time sampling as well as the

 © 2014. American Geophysical Union. All Rights Reserved.

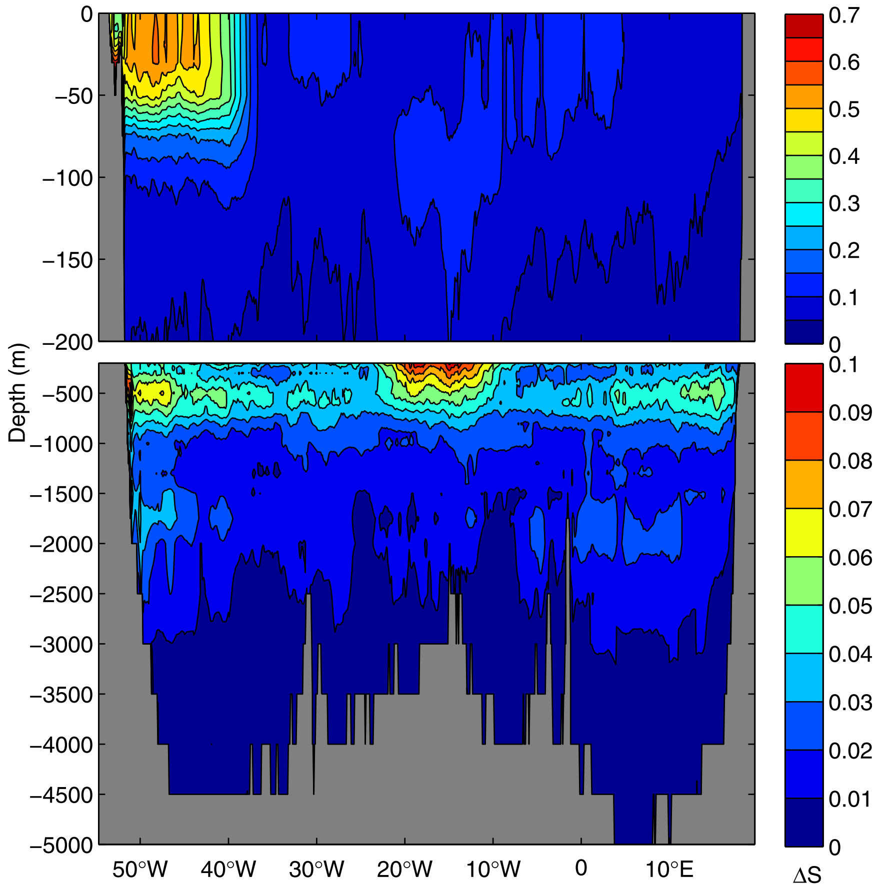

Figure 6. RMS error (psu) between the estimated salinity using climatological T-S relationships and the model salinity along the 34°S section.

year-to-year variability of number of transects may alias the estimates of the annual cycle of the AMOC and meridional heat transport [*Bryden et al*., 2005]. We simulate in the model uncertainties associated with the transect temporal sampling by randomly selecting points in the time series of the AMOC and MHT, and use the RMS difference of monthly means of these two quantities as a measure of the uncertainty associated with the temporal sampling. We vary two parameters associated with the temporal sampling of the AX18 transect: The number of realizations per year, from 1 to 20 times per year, and the number of years of data collection, from 1 to 15 years. The random sampling is calculated in three steps. First, the original time series of the AMOC and MHT are extended by padding up to 100 years. Some small stochastic noise is added to the extended time series. Seasonality is maintained in this time series by choosing accordingly the beginning of each padded time series. Second, a stretch of the 100 year time series is chosen with its length defined by the uncertain parameter number of years sampled. Third, according the number of samples per year, random samples are taken from the stretch of the time series. In this step, the samples are evenly distributed around the year, for example, with a two sample per year parameter setting, one sample is taken every semester. These steps are reproduced 400 times, which is a number sufficiently high to allow all months to be sampled and the average of all realizations to have the same monthly means as the original model AMOC and MHT. Furthermore, the sum of the first and second harmonics of the monthly means is performed for each realization, and the RMS error of the 400 realizations will define a measure of the uncertainty associated with the time sampling.

Contour plots showing the sampling error variability of the AMOC and MHT with respect to the number of years measured and the number of samples per year are shown in Figure 7. The time sampling error of the AMOC and MHT show similar behavior, i.e., errors decrease exponentially as more samples are collected during the year or when a higher number of years is sampled. The RMS errors are as low as ±0.5 Sv and ±0.05 PW when carrying out up to 12 transect realizations per year for 15 years. On the other hand, when

© 2014. American Geophysical Union. All Rights Reserved.

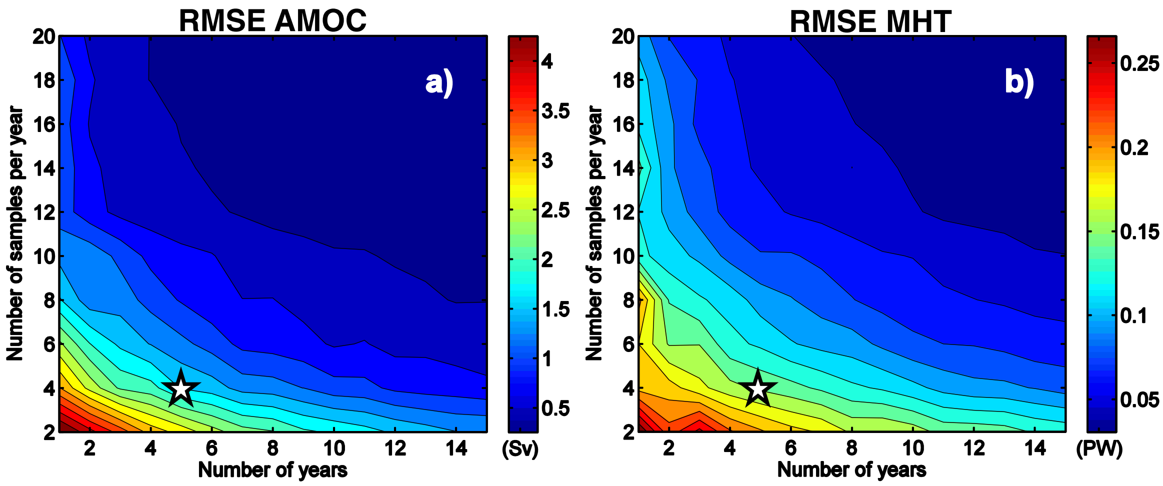

Figure 7. RMS error of the reconstructed (a) AMOC and (b) MHT associated with different time samplings, i.e., the number of samples per year (*y* axis) and the number of year (*x* axis). The RMS error is calculated from the difference between the seasonal cycles, calculated as the sum of the first and second harmonics, of the resampled time series and the time series using the original model sampling. The number of samples per year is randomly selected, and this process is realized 400 times to average the random realizations. The stars in Figures 7a and 7b correspond to the current location of the AX18 sampling in the time sampling parameter space.

transects are carried out twice a year for 2 years, the errors are above $\pm$3.5 Sv and $\pm$0.25 PW, respectively. The current number of realizations of the AX18 transect along the nominal of 34°S is 18 (Figure 2), which are done approximately on a quarterly basis. This is equivalent to a total sampling period of 5 years in our considered parameter space. Therefore, according to our model estimates, the associated RMS errors of the AMOC and MHT are $\pm$1.7 Sv and $\pm$0.15 PW, respectively (stars in Figure 7), close to the most uncertain values in the studies parameter space. Although 12 realizations per year are difficult to achieve operationally, current discussions for increasing the number of transect realizations to five or six per year are underway. This would lower the RMS errors to $<$1.5 Sv for the AMOC and $<$0.14 PW for the MHT, which may allow a greater improvement over the years.

One additional temporal sampling error arises from the nonsynopticity of the XBT transect measurements. An AX18 realization takes approximately 10 days to complete the trajectory from South America to Cape Town, which may alias the transport estimates across this transect. We quantify here the errors due to nonsynopticity by simulating the same observational assumptions within the model environment. In this experiment, we simulate one AX18 XBT realization for each model day by using 10 bins of meridional velocity values from east to west that correspond to 10 consecutive days of model velocity. The AMOC and MHT are estimated every 7 days from these simulations, using as the time tag the first day of each nonsynoptic field. These estimates are compared against the ones from the synoptic model outputs. The errors associated with the nonsynopticity of the data for the whole period of the simulation are 0.21 $\pm$ 4.1 Sv for the AMOC and 0.01 $\pm$ 0.25 PW for MHT. The RMS values due to nonsynopticity are on the same order as the RMS errors produced by the quarterly sampling. However, since this calculation is performed over model daily values instead of 7 day averages, these RMS values are actually an overestimation in comparison to the other experiments.

5.3.2. Horizontal Sampling

The AX18 XBT transect crosses three regions of different dynamic regimes (Figure 1): (i) the western (Confluence region), interior (gyre), and eastern (Agulhas leakage) regions. Previous studies suggest that it is critical to account for the variability in all three regions in order to monitor and quantify changes in the AMOC and MHT [*Dong et al*., 2009]. The current XBT spatial sampling strategy accounts for the different regional characteristics: at a lower density ($\sim$50 km) in the interior region, and at higher density ($\sim$25 km) closer to the boundaries, i.e., east of the Walvis Ridge ($\sim$1°W) and west of 40°W, outside the continental slope region in South America. This sampling strategy is a heuristic approach to add more spatial resolution to the high energy boundary regions (Figure 1). Here we quantify the sensitivity of the meridional transport changes to the horizontal sampling in these three regions. To accomplish this, we generate an ensemble with 30 members by degrading the longitudinal resolution in each of the three regions separately. Therefore, we start

© 2014. American Geophysical Union. All Rights Reserved.

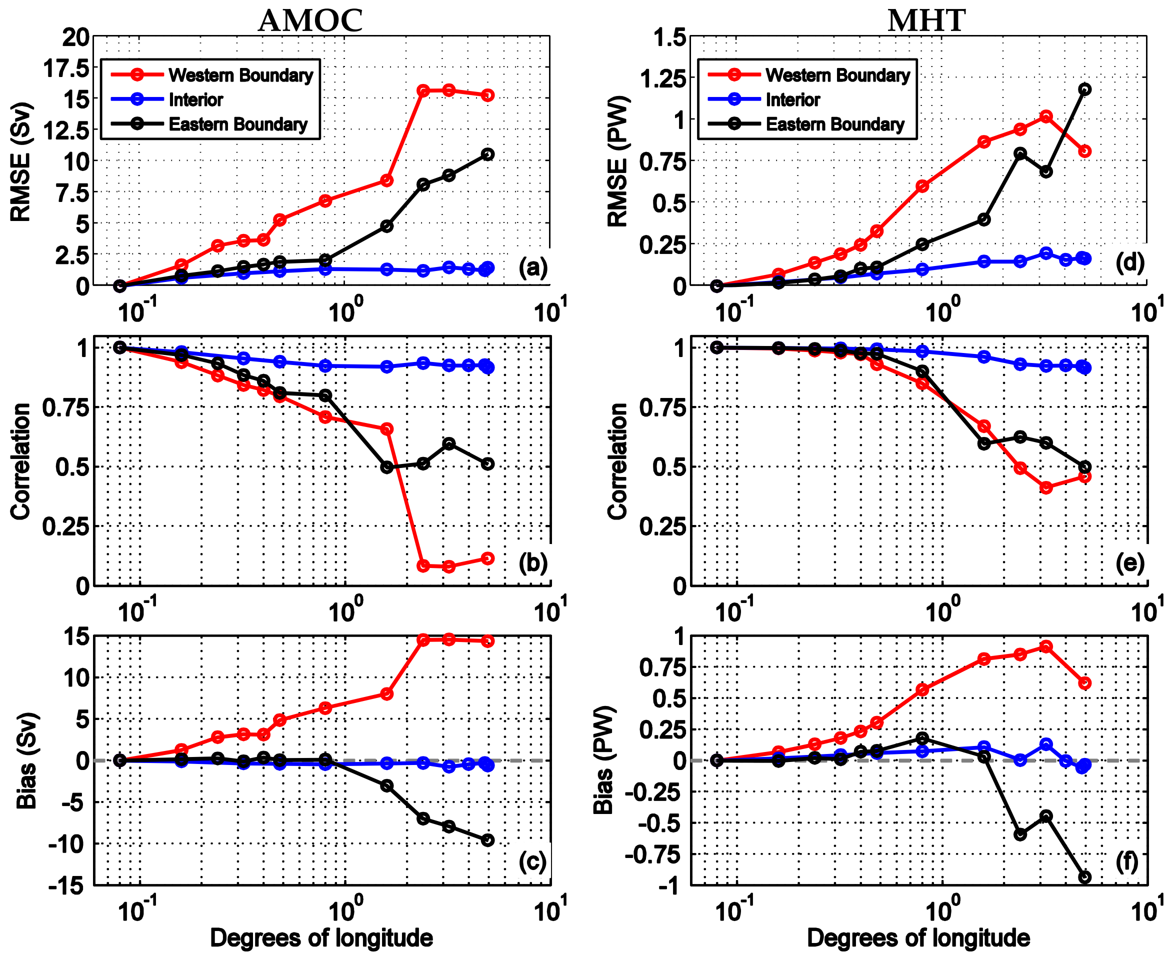

Figure 8. RMS error, correlation, and bias of the (a–c) AMOC and (d–f) MHT with respect to the simulated longitudinal resolution (in degrees) of the AX18 transect. The transect horizontal resolution varies individually for three regions, western boundary (red), interior (blue), and eastern boundary (black). The *x* axis is shown in logarithmic scale.

from the standard model resolution (0.08°; ~7.3 km) in the whole section, and degrade the sampling spacing in one of the regions keeping the others at the standard resolution. We produce 10 members for each region, at variable steps, up to a maximum 5° spacing (~460 km), giving more emphasis to the high-resolution sampling. We use the RMS error, bias, and correlation as metrics to compare the reconstructions to the original AMOC and MHT strength.

Our results show that the AMOC strength and MHT are less sensitive to changes in the spatial resolution in the interior than at the boundary regions (Figure 8). For the AMOC, degrading the resolution in the interior to a 3° longitude sampling produces a small negative bias and RMS error of -0.45 ± 1.3 Sv, and a minimum correlation of ~0.9. For a 50 km resolution (~0.6°), the error is -0.1 ± 1.1 Sv and 0.01 ± 0.06 PW. In the boundary regions, the AMOC and MHT are more sensitive to changes in spatial sampling. The bias and RMS error for a 25 km (~0.3°) spacing is of 1.7 ± 2.4 Sv/0.03 ± 0.06 PW in the western and 1.0 ± 1.4 Sv/-0.03 ± 0.04 PW in the eastern boundary. The correlation is about 0.9 at 25 km spacing in the boundaries, and decreases to 0.6 when longitudinal sampling is larger than ~90 km (1°). The larger decrease of correlation in the boundaries is partly due to subsampling of strong currents and high mesoscale activity, and also because the shelf transport may not be observed at lower sampling rates. The potentially unresolved volume transports in the continental shelves (above 200 m deep) are -0.61 ± 0.77 Sv in the west and 0.15 ± 0.44 Sv in the east of the basin. Both transports on the shelf contribute only a negligible temperature transport (~10^{-8} PW), which agrees with the estimates of *Baringer and Garzoli* [2007]. Therefore, a higher AX18 horizontal sampling is indeed needed in the eastern and western boundaries, especially in the western side of the basin, where the current sampling biases are larger in comparison to the other regions.

© 2014. American Geophysical Union. All Rights Reserved.

Interestingly, biases in the MHT have opposite signs and similar magnitudes when comparing the western and eastern boundaries for any given zonal sampling resolution (Figures 8c and 8f). Therefore, biases in the eastern and western regions may cancel each other to some extent. The opposite bias signals in the eastern and western side of the basin arises because at lower resolutions, the reconstruction cannot resolve well the northward Benguela Current and the southward Brazil Current, producing a negative volume transport bias in the east and positive transport bias in the west.

5.4. AMOC and MHT Uncertainties Due to Computational Methodology

In the previous section, we analyzed the sensitivity of the AMOC and MHT to strategies for different temporal and spatial sampling of the AX18 XBT transect. In this section, we investigate how methodological assumptions affect the AMOC and MHT estimated at 34°S. First, we will explore the impact of salinity and deep temperature inferences. Additionally, we optimize the choice of the reference level, and propose a method to estimate the barotropic velocities across the transect.

5.4.1. Salinity and Deep Temperature Inferences

To study the impact of salinity and deep temperature inferences on the AMOC and MHT, we perform step changes in the model observational strategy. We reconstruct Ψ_y and MHT using: (i) the constructed annual T-S lookup table (section 5.1) to estimate salinity profiles in the upper 800 m, (ii) padding the model T-S monthly climatology in the deep ocean (>800 m deep), and (iii) using both the lookup table in the upper ocean and padding in the deeper ocean.

We compare the changes in the reconstructed AMOC strength and MHT using these approximations against those calculated using the full model T-S fields. The main variability of the AMOC and MHT follow closely the ones from the approximated fields (not shown). The analysis of the residuals relative to the reconstructions using the full model fields (Figure 9) show that, although error amplitudes are similar, the T-S lookup approximation drives most of the mean residual AMOC changes (0.32 ± 1.4 Sv). In addition, the residuals from the T-S lookup approximation are subject to strong seasonality. Biases in AMOC strength can reach −1 Sv during austral winter and 1 Sv during summer. This seasonal bias is due to the fact that the T-S relationships are taken from an annual mean. Deep ocean padding biases do not show clear seasonality, and AMOC and MHT mean biases are small, with magnitude of −0.02 ± 1.7 Sv. The total AMOC error is 0.3 ± 2.3 Sv, approximately 2% of the AMOC signal. For the MHT (Figure 9b), performing either padding or TS lookup approximations produce residual changes of 0 ± 0.09 PW and 0.06 ± 0.12 PW, respectively. These total RMS errors calculated are similar to the ones calculated the value of ±0.03 PW and ±0.15 estimated for these approximations using the cumulative transport of the WOCE A10 section considered in *Baringer and Garzoli* [2007]. The results of our analysis using a 6 year time series show that although the errors produced by salinity and deep temperature approximations are similar in value, the seasonal amplitude of the MHT and AMOC residuals using the TS lookup table is the largest (right plots in Figures 9a and 9b). Although these are conservative estimates, given that the model climatology represents well the variability below the surface, the errors caused by deep T-S padding are small in comparison to the other sources. Thus, deployment of a whole water column CTD is not essential for a strong reduction of errors in the AX18 XBT transect.

5.4.2. Reference Velocities for Geostrophic Velocity Calculation

As indicated from the model output (Figure 10), variations in bottom topography are the main driver of strong barotropic velocities at 34°S. Previous studies suggest that the barotropic mode accounts for most of the bias of the overturning circulation [*Baehr et al*., 2004, 2009; *Rayner et al*., 2011] in zonal section with steep bottom topography, which could be introduced by assuming an inaccurate reference velocities. *Baehr et al*. [2009] estimate a 9 Sv bias if a level of no motion is assumed at the ocean bottom along 35°S.

Here we perform four experiments to estimate the sensitivity of the reconstructed AMOC to a possible knowledge about the reference level velocity: (a) with zero reference velocities, and with climatological reference velocities, (b) at the western boundary only, (c) at the eastern boundary only, and (d) at both western and eastern boundaries. Similar to observational studies, we assume in all experiments a constant reference depth along $\sigma_2=37.09$, and test the knowledge of climatological velocities at different locations along this reference level. We compare the resulted geostrophic component of the AMOC against the perfect model reconstruction (section 2), which using the full model velocities at the reference level.

Figure 11 shows the evolution of the geostrophic component of the AMOC stream function (left plots) for the experiments (a–d), and their respective time-mean contributions to the geostrophic component (vertical shear and barotropic) is compared to the perfect model reconstruction (right plots).

© 2014. American Geophysical Union. All Rights Reserved.

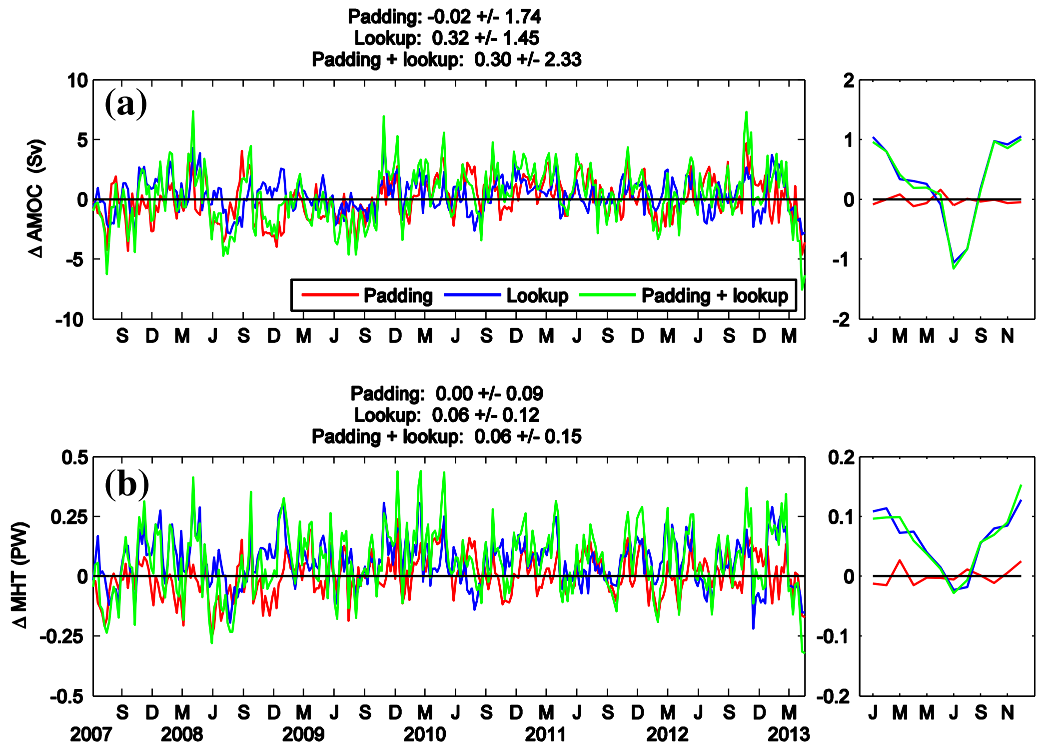

Figure 9. Residual time series relative to the reconstruction using the total T-S model field of (a) AMOC and (b) MHT, and respective monthly averages (right plots). The colored time series are for the reconstructions using a bottom T-S climatology padding (red), salinity inference from lookup table in the top 800 m (blue), and padding plus T-S lookup (green).

From the evolution of the geostrophic component of the AMOC stream function in these experiments, we can observe that the AMOC is stronger, often above 20 Sv in Figure 11a, when less information is known about the reference velocity. This result is explained by the decomposition of the geostrophic stream function. As previously shown in Figure 3, the barotropic stream function (Ψ_{bar}) is the main balance of the

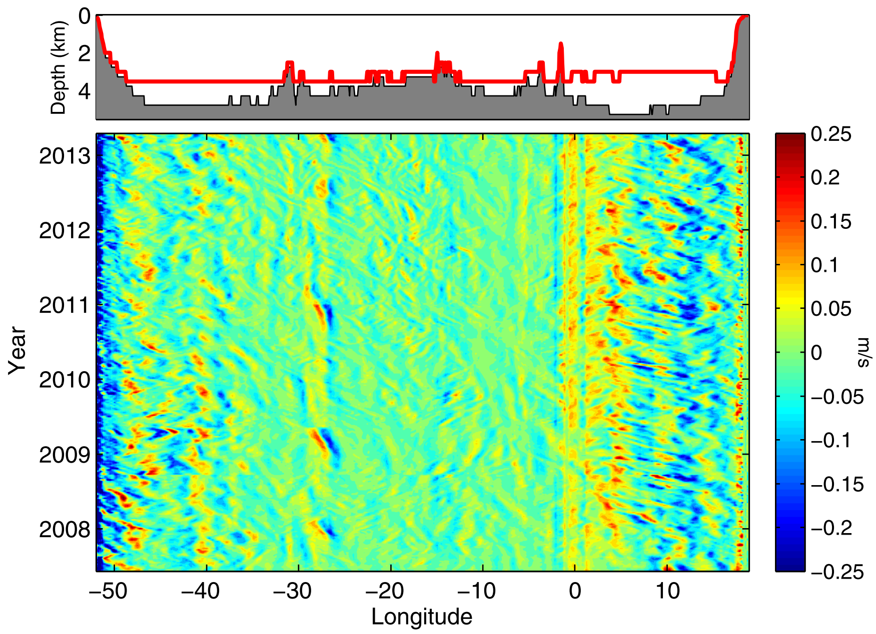

Figure 10. Barotropic velocities at 34.5°S estimated from the model velocities. The top plot shows the average depth of the σ_2=37.09 (red line) overlaid on model bathymetry.

© 2014. American Geophysical Union. All Rights Reserved.

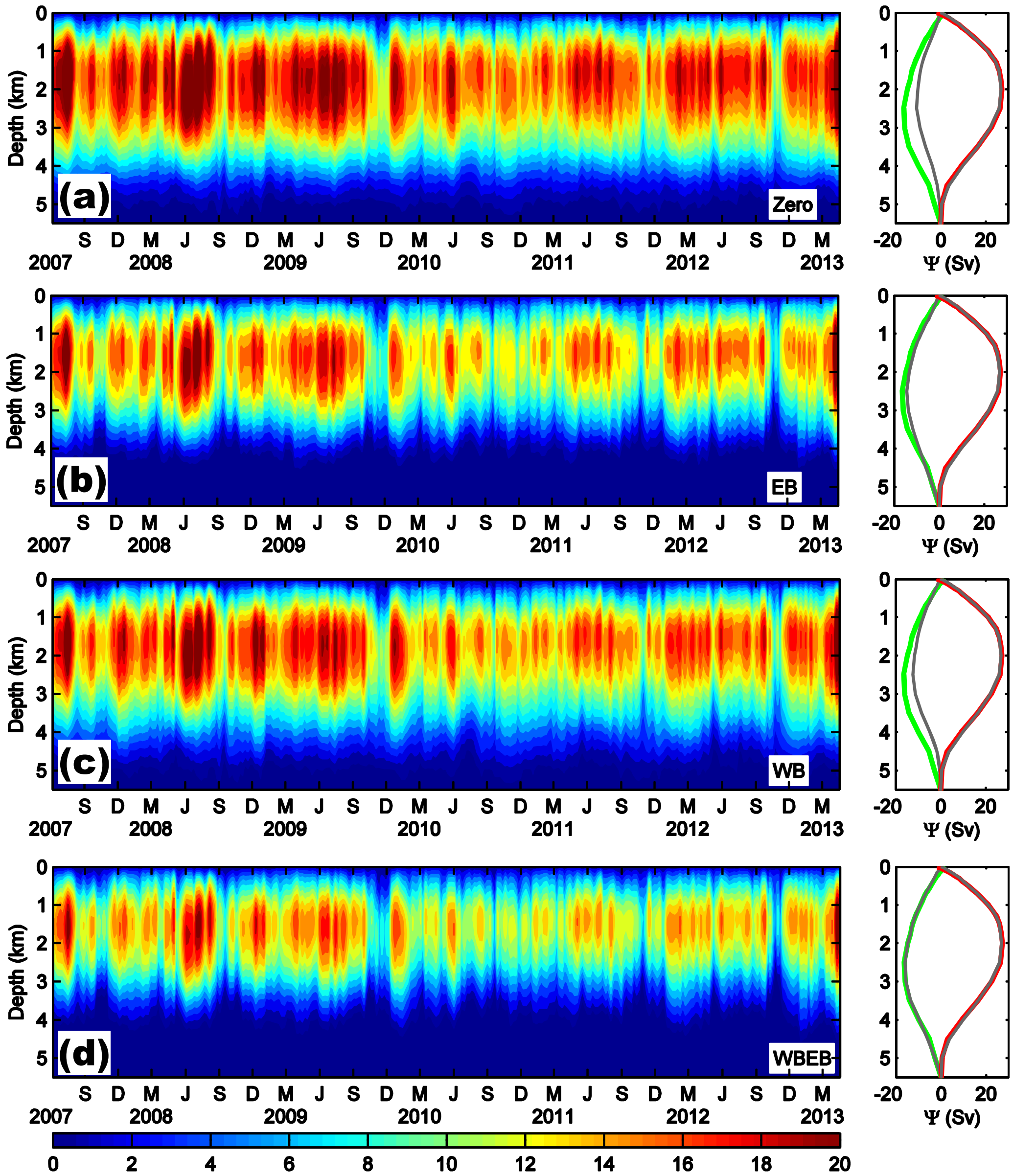

Figure 11. Sensitivity of the AMOC stream function (Sv) due to the knowledge of a climatological reference velocity at $\sigma_2 = 37.09$. (a) Zero reference velocity, (b) eastern boundary, (c) western boundary, and (d) western plus eastern boundaries. (left) Time evolution of the geostrophic contribution to the AMOC stream function. (right) Time average of the barotropic (green) and the vertical shear (red) stream function components assuming perfect knowledge of velocities, and the gray lines are the respective reconstructions for each of the components using the four approximations.

vertical shear component in the model. In the present experiments, the vertical shear component is highly unaffected by the choice of reference velocities, since they are estimated at the same depth. Therefore, a weaker Ψ_{bar}, as shown in Figure 11a acts to increase the AMOC strength, since the vertical shear component is highly unaffected by the choice of reference velocities.

When using the full model velocities at the reference level, the reconstructed Ψ_{bar} has a mean strength of -16.3 Sv. When zero reference velocity is assumed, a much weaker Ψ_{bar} strength value is estimated ($\Psi_{bar} = -10.5$ Sv; Figure 11a), causing a mean bias of the geostrophic contribution to the AMOC strength of 5.7 ± 4.4 Sv, and also increases the MHT by 0.17 ± 0.16. Adding a climatological reference velocity in the boundaries reduces the uncertainties in the barotropic mode. The derived AMOC strength estimates using climatological reference velocities in the boundaries produce positive biases of 4.0 ± 4.5 Sv (0.06 ± 0.16 PW) in the western boundary and 2.0 ± 4.3 Sv (0.10 ± 0.14 PW) in the eastern side of the basin (Figures 11b

© 2014. American Geophysical Union. All Rights Reserved.

and 11c, respectively). Therefore, the eastern boundary velocity information reduces uncertainties more than in the western boundary. When both eastern and western reference velocities are added (Figure 11d), the mean $\Psi_{bar} = -16.0$ Sv, and the AMOC strength is accurately measured at a value of 0.3 ± 4.4 Sv (-0.02 ± 0.14 PW). Further adding reference velocity information in the interior does not improve these uncertainty values.

Therefore, we show here that the misrepresentation of the reference velocities in the geostrophic calculation yields the highest contribution to the uncertainties in the AMOC and MHT calculations. Knowledge of the reference level velocities at both the western and eastern boundaries is necessary for considerably reducing the mean bias in the barotropic mode. This can be achieved by using climatological values in the boundaries, and this information may be acquired from available Argo float climatologies [e.g., *Goes et al.*, 2013], for example. Although the vertical shear component is unaffected by the reference velocity, and climatological reference velocities produce small mean biases in the AMOC and MHT estimates (0.3 Sv and -0.02 PW, respectively), there is still strong uncertainty in the lower frequency variability of the barotropic transport, given by their RMS error, which are ± 4.4 Sv and ± 0.14 PW. To resolve the variability of the barotropic mode, additional available observations can be used. This question is addressed in the next section.

5.4.3. Alternative Barotropic Velocity Estimation Using Altimetry and Hydrography

In order to optimize the information necessary to monitor the AMOC at 34°S, several additional observations could be used to complement the AX18 XBT transect measurements. Some complimentary observations are already in place, such as the satellite wind stress measurements used to estimate the Ekman transport.

A topic of current research in the AMOC decomposition is the estimation of the barotropic mode. In an XBT system, where climatology is assumed below 800 m, using a reference level near the bottom of the ocean prevents capturing interannual or longer variability due to the presence of deep flows. Bottom pressure (P_{bot}) recorders are a useful platform to compute the time varying reference level for the meridional geostrophic velocity, and, therefore, estimate the nonsteric component of the sea level height (SLH). Such a platform requires further investment in an array across the basin, and efforts are underway [*Perez et al.*, 2011; *Meinen et al.*, 2012]. Some recent studies use a blend of altimetry and Argo parking velocity as the reference level or level of known motion to infer absolute geostrophic velocities [*Willis and Fu*, 2008; *Mielke et al.*, 2013; *Goes et al.*, 2013]. However, because a large number of Argo floats is necessary to produce a reliable estimate across the basin, seasonal averages are generally used in an Argo-based reference level. We showed in the previous section that a climatological assumption of the reference velocity in the eastern and western boundaries can reduce the AMOC mean bias significantly. Here we test another method for measuring the barotropic flow by using SLH derived from satellite altimetry in conjunction with hydrographic data. Altimetry captures both steric and nonsteric components, whose contributions are variable among different regions of the ocean [*Guinehut et al.*, 2006]. The nonsteric contribution generally increases toward higher latitudes due to weaker stratification and stronger Coriolis force. In some regions the nonsteric contributions, such as the barotropic component, can account for more than 50% of the total sea level variability [*Shriver and Hurlburt*, 2000].

Using the hydrostatic relation, the total sea level can be accurately related to bottom and atmospheric (P_{atm}) pressure, plus the steric contribution [*Park and Watts*, 2005], respectively $\mathrm{SLH} = (P_{bot} - P_{atm} - \rho_0 g H)/\rho_0 g$. In order to estimate the nonsteric (P_{bot}) component of the sea level, we remove the steric contribution by calculating the residual between SLH and the dynamic height (DH) referenced at a certain level (SLH – DH). The mean over the whole section is subtracted from the residuals. The barotropic velocities are calculated using geostrophy on this residual field after the zonal mean is subtracted from this field. The AMOC and MHT reconstructions are then performed assuming a level of known motion at the same reference depth as DH, and use the derived barotropic velocities as the reference velocities at that depth. Finally, we compare the results of this reconstruction against the perfect reconstruction performed in section 5.1. In addition, we test the sensitivity of the choice of reference level in this calculation, varying the depth of the reference level from the surface to the bottom of the ocean, similarly to the analysis performed in *Baehr et al.* [2009].

Figures 12a–12c show the error parameters (correlation, bias, and RMS error) of the AMOC stream function relative to the depth of the profile and the reference level adopted in the geostrophic calculations. The error

© 2014. American Geophysical Union. All Rights Reserved.

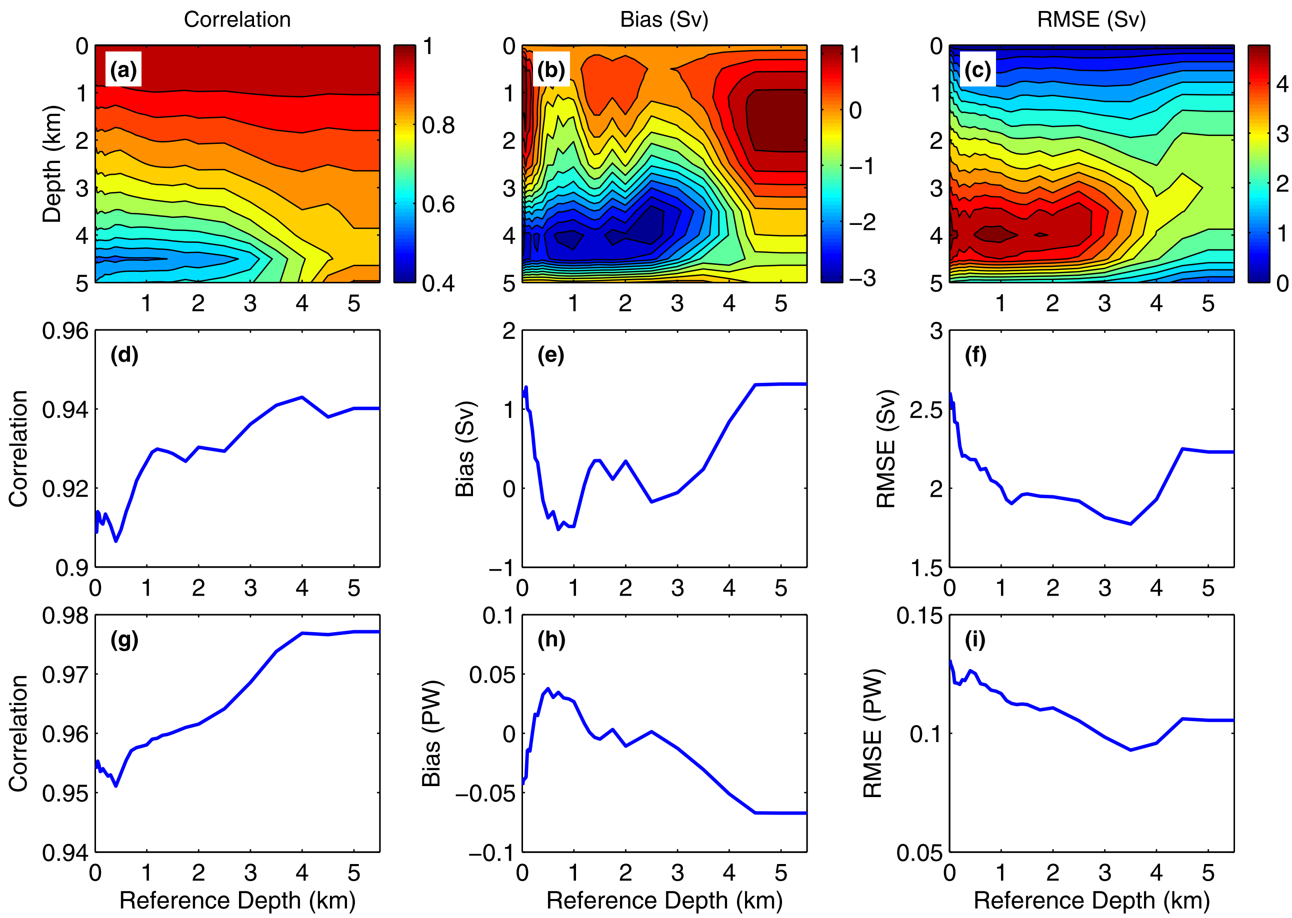

Figure 12. (a) Correlation, (b) bias (Sv), and (c) RMS error (Sv) over depth (*y* axis) of the AMOC stream function reconstruction using a variable reference depth (*x* axis) for the geostrophic calculations and a reference velocity estimated from the altimetry-dynamic height residuals. Correlation, bias, and RMS error of the (d–f) AMOC strength in Sv and (g–i) MHT in PW relative to the reference depth. All errors are calculated against the AMOC/MHT perfect reconstruction using the model reference velocities at the bottom of the ocean.

parameters show that when a shallow reference level is assumed, large errors are produced in the deep part of the stream function (>3000 m). Negative stream function biases may reach up to 3 Sv around 4000 m (Figure 12b). Using a reference level below 3000 m reduces significantly the deep biases to below 1 Sv, and improves correlations to above 0.8. Using a reference level deeper that 4500 m produces a positive AMOC bias of 1 Sv in the shallower locations, close to the maximum stream function (Figure 3), although correlation and RMS error seem to stabilize at those depths. In this analysis, the errors affecting the AMOC strength and MHT (Figures 12d–12i) generally hit a minimum close to 3700 m, which is approximately the $\sigma_2=37.09$ depth where there is the inversion of the total stream function sign (Figure 3). At this depth, the correlations are above 0.94 for both AMOC and MHT (Figures 12d and 12g), and the biases are 0.6 ± 1.8 Sv and -0.04 ± 0.09 PW, respectively. Therefore, this result confirms findings of previous observational studies [*Ganachaud and Wunsch*, 2003; *Dong et al*., 2009] that the choice of a reference level at approximately 3700 m is the most appropriate. Finally, we quantify how much information is gained for using the altimetry residual velocity as a reference for barotropic velocity. As derived in the previous section, the cases with a level of no motion or a climatological reference level at $\sigma_2=37.09$ show a correlation with the perfect reconstruction of approximately 0.74, and RMS errors of $\pm$4.4 Sv and $\pm$0.16 PW. Therefore, no gain exists in the AMOC variability estimation by applying these two different assumptions. The bias, however, as found in Figure 11, decreases considerably (from 5.7 to 0.3 Sv, and 0.17 to 0.06 PW) when applying a climatological reference level in the boundaries. When using altimetry with a reference level at 3700 m, there is a gain of 0.2 in correlation and a reduction of 5 Sv and 0.1 PW in the bias, and 2.6 Sv and 0.07 PW in the RMS error, when compared to a level of no motion. Therefore, these results are a proof of concept that altimetry and XBT data are complementary platforms to reduce for the inference of the long-term variability of the AMOC.

© 2014. American Geophysical Union. All Rights Reserved.

6. Conclusions

In this study, we use a high-resolution model assimilation product to assess the observational and computational uncertainties associated with estimating meridional transports using the data from the AX18 XBT transect along 34°S. We analyzed the AMOC and MHT in terms of their vertical shear, barotropic, and Ekman components. These terms are here used to reconstruct the AMOC and MHT. We show that this method is well suited for this type of work. In comparison to the AMOC calculated from the model velocities, the reconstructed AMOC stream function is able to represent the main model features. All error estimates here are for daily to weekly averages, and some of the high frequency variability such as nonlinear and ageostrophic eddy signals cannot be captured by the reconstruction. These randomness of these errors tend to average out on longer time scales.

A rough estimate of the total errors, assuming they are normally distributed and independent, associated with the XBT computational and operational approximations in a daily to 7 day time scales is 0.8 ± 11 Sv and 0.01 ± 0.52 Sv, for the AMOC and MHT, respectively. These errors are in the same order of magnitude of errors associated with other observational platforms at 34°S [*Meinen et al*., 2013]. A key finding obtained here is that XBTs produce acceptable estimates of the AMOC and MHT variability, where the uncertainties obtained by the multiple sources of error are smaller than the signal of the time series variability. In addition, we show that data from other platforms such as Argo and satellite altimetry can improve these errors considerably. Therefore, the AX18 transect is a valuable and longstanding piece of a multiple platform monitoring system for the region, and efforts should be made to maintain and improve it. The results obtained here are summarized in Table 1, and the results of *Baringer and Garzoli* [2007] for MHT are added for comparison. As follows, we make recommendations for optimization of sampling and computational methodologies to improve estimates of the AMOC and meridional MHT:

1. Current quarterly sampling causes an average RMS error of ±1.7 Sv and ±0.15 PW in the climatological AMOC and MHT estimates, respectively. The optimal strategy to reduce this sampling error would be to carry out 12 transects per year, i.e., one per month, which is not feasible due to operational constraints. More realistically, it is desirable to conduct continuous realizations at current quarterly sampling for at least 15 years.

2. Spatial subsampling in the interior produces small errors in the AMOC and MHT estimates compared to the errors produced at the boundaries. The current AX18 zonal sampling uses 25 km on the boundaries and 50 km in the interior of the basin. This current spatial sampling seems to be adequate to capture most of the variability of the meridional transports, although the western boundary resolution still shows large AMOC bias at the present sampling (1.7 ± 2.4 Sv). An increase in the western boundary sampling to 20 km would improve the accuracy of the current AMOC calculations by ~1 Sv.

3. The effect of T-S padding of monthly climatology below 800 m on the AMOC (−0.02 ± 1.7 Sv) and MHT (0.0 ± 0.09) estimates is relatively small in comparison to the other error sources. The effect of using salinity from the T-S lookup table in the upper 800 m is also small in comparison to the other components, and is about the same order as the deep ocean padding. However, seasonal biases in the annual climatology can produce AMOC monthly biases of as much as 1 Sv. Salinity from other measurements, such as Argo, can produce monthly climatologies of T-S relationships, which would in principle avoid these seasonal biases.

4. As described in previous studies [e.g., *Kanzow et al*., 2007], (for 26.5°N), the barotropic mode is likely to be the most

Table 1. Bias ± RMS Error of the AMOC (Sv) and MHT (PW) Introduced by Each Source of Error Associated With the AX18 XBT Transect Observational Assumptions Estimated in the Present Study[a]

	AMOC (Sv)	Meridional Heat Transport (PW)	
Source	Present	Present	B&G
Upper ocean salinity	0.32 ± 1.4	0.06 ± 0.12	0.03
Deep climatology below 800 m	−0.02 ± 1.7	0.0 ± 0.09	0.15
Mass imbalance	0.9 ± 3.8	−0.02 ± 0.06	0.02
Nonsynopticity	0.2 ± 4.1	0.01 ± 0.25	
Ageostrophic eddies (non-Ekman)	0.6 ± 5.5	−0.06 ± 0.32	0.05
Quarterly sampling	0 ± 1.7	0 ± 0.15	
Unresolved western shelf transport	−0.6 ± 0.8	10^{-8}	0.01
Unresolved eastern shelf transport	0.15 ± 0.4	10^{-8}	0.01
Western horizontal resolution (25 km)	1.7 ± 2.4	0.03 ± 0.06	
Eastern horizontal resolution (25 km)	1.0 ± 1.4	−0.03 ± 0.04	
Interior horizontal resolution (50 km)	−0.1 ± 1.1	0.01 ± 0.06	
Western reference velocity	4.0 ± 4.5	0.06 ± 0.16	0.02
Eastern reference velocity	2.0 ± 4.3	0.10 ± 0.14	
Reference level depth	0.6 ± 1.8	−0.04 ± 0.09	0.05

[a]Last column shows the biases estimates of *Baringer and Garzoli* [2007, Table 3].

 © 2014. American Geophysical Union. All Rights Reserved.

significant source of error in the AMOC and MHT calculations due to the extensive continental shelf along 34°S. The best location for a level of no motion is around 3700 m, approximately the depth of σ_2=37.09 kg m^{-3}. However, errors are on the order of 5.7 ± 4.4 Sv for the AMOC and 0.17 ± 0.16 PW for MHT if a level of no motion is used in σ_2=37.09 kg m^{-3}. Using at least climatological values as the reference velocities in both boundaries is necessary to reduce the AMOC and MHT mean biases to ~0.3 ± 4.4 Sv and 0.02 ± 0.14 PW, respectively.

5. The use of satellite altimetry observations in conjunction with hydrographic data is a good alternative for barotropic component of the AMOC/MHT. We show that errors in the barotropic mode estimation using the non-steric component of altimetry are 0.6 ± 1.8 Sv and -0.04 ± 0.09 PW, an improvement of up to 90% in the bias and and 60 % in the RMS in comparison to the commonly used level of no motion at σ_2=37.09 kg m^{-3}.

Finally, this study assesses only one the part of the several platforms that are in place to monitor the variability of the AMOC and MHT in the South Atlantic, XBT and altimetry data. The utility of the other operational platforms, such as moorings and Argo data, has been demonstrated in various other studies [*Dong et al*., 2011b; *Perez et al*., 2011]. An analysis that includes a blend of several platforms is still necessary to evaluate an optimal observational system for the region.

Acknowledgments
The data used in this study are available in the following websites: the model assimilation runs at www.hycom.org, WOA05 temperature data at www.nodc.noaa.gov/OC5/WOA05/woa05data.html, AX18 transect data at www.aoml.noaa.gov/phod/hdenxbt/ax_home.php?ax=18, and SLA data at www.aviso.com. The authors want to thank Joe Metzger for providing the GLBa0.08/74.2 simulation output, Molly Baringer for scientific discussions, Johanna Baher for help with the AMOC reconstruction calculations, and the ship companies for carrying out the AX18 cruises as part of the Ships of Opportunity project. This research was accomplished under the auspices of the Cooperative Institute for Marine and Atmospheric Studies (CIMAS), a cooperative institute of the University of Miami and the National Oceanic and Atmospheric Administration, cooperative agreement NA17RJ1226, and was partly funded by the NOAA Climate Program Office.

References

Ansorge, I. J., et al. (2014), Basin-wide oceanographic array bridges the South Atlantic, *Eos Trans. AGU*, *95*(6), 53–54.

Baehr, J., J. Hirschi, J.-O. Beismann, and J. Marotzke (2004), Monitoring the meridional overturning circulation in the North Atlantic: A model-based array design study, *J. Mar. Res.*, *62*(3), 283–312, doi:10.1357/0022240041446191.

Baehr, J., D. McInerney, K. Keller, and J. Marotzke (2008), Optimization of an observing system design for the North Atlantic meridional overturning circulation, *J. Atmos. Oceanic Technol.*, *25*(4), 625–634, doi:10.1175/2007JTECHO535.1.

Baehr, J., A. Stroup, and J. Marotzke (2009), Testing concepts for continuous monitoring of the meridional overturning circulation in the South Atlantic, *Ocean Modell.*, *29*, 147–153.

Baringer, M., and S. Garzoli (2007), Meridional heat transport determined with expendable bathythermographs. Part I: Error estimates from model and hydrographic data, *Deep Sea Res., Part I*, *54*(8), 1390–1401, doi:10.1016/j.dsr.2007.03.011.

Beal, L. M., W. P. M. D. Ruijter, A. Biastoch, R. Zahn, and SCOR/WCRP/IAPSO Working Group 136 (2011), On the role of the Agulhas system in ocean circulation and climate, *Nature*, *472*(7344), 429–436, doi:10.1038/nature09983.

Biastoch, A., C. W. Böning, F. U. Schwarzkopf, and J. R. E. Lutjeharms (2009), Increase in Agulhas leakage due to poleward shift in the southern hemisphere westerlies, *Nature*, *462*, 495–498, doi:10.1038/nature08519.

Boening, C., T. Lee, and V. Zlotnicki (2011), A record-high ocean bottom pressure in the South Pacific observed by GRACE, *Geophys. Res. Lett.*, *38*, L04602, doi:10.1029/2010GL046013.

Bryden, H. L., H. R. Longworth, and S. A. Cunningham (2005), Slowing of the Atlantic meridional overturning circulation at 25°N, *Nature*, *438*, 655–657, doi:10.1038/nature04385.

Chassignet, E., et al. (2009), U.S. GODAE: Global ocean prediction with the hybrid coordinate ocean model (HYCOM), *Oceanography*, *22*(2), 64–75, doi:10.5670/oceanog.2009.39.

Cummings, J. A. (2005), Operational multivariate ocean data assimilation, *Q. J. R. Meteorol. Soc.*, *131*(613), 3583–3604, doi:10.1256/qj.05.105.

Dong, B.-W., and R. T. Sutton (2007), Enhancement of El Nino-Southern Oscillation ENSO variability by a weakened Atlantic thermohaline circulation in a coupled GCM, *J. Clim.*, *20*, 4920–4939, doi:10.1016/j.dsr2.2010.10.069.

Dong, S., S. L. Garzoli, M. O. Baringer, C. S. Meinen, and G. J. Goni (2009), Interannual variations in the Atlantic meridional overturning circulation and its relationship with the net northward heat transport in the South Atlantic, *Geophys. Res. Lett.*, *36*, L20606, doi:10.1029/2009GL039356.

Dong, S., S. Garzoli, and M. Baringer (2011a), The role of interocean exchanges on decadal variations of the meridional heat transport in the South Atlantic, *J. Phys. Oceanogr.*, *41*, 1498–1511, doi:10.1175/2011JPO4549.1.

Dong, S., M. Baringer, G. Goni, and S. Garzoli (2011b), Importance of the assimilation of Argo float measurements on the meridional overturning circulation in the South Atlantic, *Geophys. Res. Lett.*, *38*, L18603, doi:10.1029/2011GL048982.

Dong, S., M. O. Baringer, G. J. Goni, C. S. Meinen, and S. L. Garzoli (2014), Seasonal variations in the South Atlantic meridional overturning circulation from observations and numerical models, *Geophys. Res. Lett.*, *41*, 4611–4618, doi:10.1002/2014GL060428.

Donners, J., and S. S. Drijfhout (2004), The Lagrangian view of South Atlantic interocean exchange in a global ocean model compared with inverse model results, *J. Phys. Oceanogr.*, *34*, 1019–1035, doi:10.1175/1520-0485(2004)034<1019:TLVOSA>2.0.CO;2.

Ducet, N., P.-Y. L. Traon, and G. Reverdin (2000), Global high-resolution mapping of ocean circulation from Topex/Poseidon and ERS-1 and −2, *J. Geophys. Res.*, *105*, 19,477–19,498, doi:10.1029/2000JC900063.

Enfield, D. B., A. M. Mestas-Nuñez, and P. J. Trimble (2001), The Atlantic Multidecadal Oscillation and its relation to rainfall and river flows in the continental U.S., *Geophys. Res. Lett.*, *28*, 2077–2080, doi:10.1029/2000GL012745.

Fox, D., W. J. Teague, C. N. Barron, M. R. Carnes, and C. M. Lee (2002), The modular ocean data assimilation system (MODAS), *J. Atmos. Oceanic Technol.*, *19*, 240–252, doi:10.1175/1520-0426(2002)019<0240:TMODAS>2.0.CO;2.

Ganachaud, A., and C. Wunsch (2003), Large scale ocean heat and freshwater transports during the World Ocean Circulation Experiment, *J. Clim.*, *16*, 696–705, doi:10.1175/1520-0442(2003)016<0696:LSOHAF>2.0.CO;2.

Garzoli, S. (1993), Geostrophic velocities and transport variability in the Brazil/Malvinas confluence, *Deep Sea Res., Part I*, *40*, 1379–1403, doi:10.1016/0967-0637(93)90118-M.

Garzoli, S., and M. Baringer (2007), Meridional heat transport determined with expendable bathythermographs. Part II: South Atlantic transport, *Deep Sea Res., Part I*, *54*, 1402–1420, doi:10.1016/j.dsr.2007.04.013.

Garzoli, S., M. Baringer, S. Dong, R. Perez, and Q. Yao (2013), South Atlantic meridional fluxes, *Deep Sea Res., Part I*, *71*, 21–32, doi:10.1016/j.dsr.2012.09.003.

© 2014. American Geophysical Union. All Rights Reserved.

Garzoli, S. L., and R. Matano (2011), The South Atlantic and the Atlantic meridional overturning circulation, *Deep Sea Res., Part II*, *58*(17–18), 1837–1847, doi:10.1016/j.dsr2.2010.10.063.

Goes, M., N. M. Urban, R. Tonkonojenkov, M. Haran, A. Schmittner, and K. Keller (2010), What is the skill of ocean tracers in reducing uncertainties about ocean diapycnal mixing and projections of the Atlantic meridional overturning circulation?, *J. Geophys. Res.*, *115*, C12006, doi:10.1029/2010JC006407.

Goes, M., G. Goni, V. Hormann, and R. Perez (2013), Variability of the Atlantic off-equatorial eastward currents during 1993–2010 using a synthetic method, *J. Geophys. Res. Oceans*, *118*, 3026–3045, doi:10.1002/jgrc.20186.

Goni, G., and I. Wainer (2001), Investigation of the Brazil Current front variability from altimeter data, *J. Geophys. Res.*, *106*, 31,117–31,128, doi:10.1029/2000JC000396.

Goni, G., S. Garzoli, A. Roubicek, D. Olson, and O. Brown (1997), Agulhas ring dynamics from TOPEX/POSEIDON satellite altimeter data, *J. Mar. Res.*, *55*(5), 861–883, doi:10.1357/0022240973224175.

Goni, G., F. Bringas, and P. D. Nezio (2011), Observed low frequency variability of the Brazil Current front, *J. Geophys. Res.*, *116*, C10037, doi:10.1029/2011JC007198.

Gordon, A. (1986), Interocean exchange of thermocline water, *J. Geophys. Res.*, *91*, 5037–5046, doi:10.1029/JC091iC04p05037.

Griffies, S. M., M. J. Harrison, R. C. Pacanowski, and A. Rosati (2004), A technical guide to MOM4, GFDL Ocean Group, *Tech. Rep. 5*, NOAA/GFDL, Princeton, N. J.

Guinehut, S., P.-Y. L. Traon, and G. Larnicol (2006), What can we learn from global altimetry/hydrography comparisons?, *Geophys. Res. Lett.*, *33*, L10604, doi:10.1029/2005GL0255551.

Hall, M. M., and H. L. Bryden (1982), Direct estimates and mechanisms of ocean heat transport, *Deep Sea Res., Part A*, *29*(3), 339–359, doi:10.1016/0198-0149(82)90099-1.

Hatun, H., A.-B. Sandø, H. Drange, B. Hansen, and H. Valdimarsson (2005), Influence of the Atlantic subpolar gyre on the thermohaline circulation, *Science*, *309*, 1841–1844, doi:10.1126/science.1114777.

Hawkings, E., R. S. Smith, L. C. Allison, J. M. Gregory, T. J. Woollings, H. Pohlmann, and B. de Cuevas (2011), Bistability of the Atlantic overturning circulation in a global climate model and links to ocean freshwater transport, *Geophys. Res. Lett.*, *38*, L10605, doi:10.1029/2011GL047208.

Hirschi, J., and J. Marotzke (2007), Reconstructing the meridional overturning circulation from boundary densities and the zonal wind stress, *J. Phys. Ocean.*, *37*, 743–763, doi:10.1175/JPO3019.1.

Hirschi, J., J. Baehr, J. Marotzke, J. Stark, S. Cunningham, and J.-O. Beismann (2003), A monitoring design for the Atlantic meridional overturning circulation, *Geophys. Res. Lett.*, *30*(7), 1413, doi:10.1029/2002GL016776.

Hu, A., G. A. Meehl, W. Han, and J. Yin (2011), Effect of the potential melting of the Greenland ice sheet on the meridional overturning circulation and global climate in the future, *Deep Sea Res., Part II*, *58*, 1914–1926, doi:10.1029/2000GL012745.

Jayne, S. R., and J. Marotzke (2001), The dynamics of ocean heat transport variability, *Rev. Geophys.*, *39*, 385–411, doi:10.1029/2000RG000084.

Kanzow, T., S. A. Cunningham, D. Rayner, J. J.-M. Hirschi, W. E. Johns, M. O. Baringer, H. L. Bryden, L. M. Beal, C. S. Meinen, and J. Marotzke (2007), Observed flow compensation associated with the MOC at 26.5 degrees N in the Atlantic, *Science*, *317*(5840), 938–941, doi:10.1126/science.1141293.

Lee, T., and J. Marotzke (1998), Seasonal cycles of meridional overturning and heat transport of the Indian Ocean, *J. Phys. Oceanogr.*, *28*, 923–943, doi:10.1175/1520-0485(1998)028<0923:SCOMOA>2.0.CO;2.

Lentini, C., G. Goni, and D. Olson (2006), Investigation of Brazil Current rings in the confluence region, *J. Geophys. Res.*, *111*, C06013, doi:10.1029/2005JC002988.

Levermann, A., A. Griesel, M. Hofmann, M. Montoya, and S. Rahmstorf (2005), Dynamic sea level changes following changes in the thermohaline circulation, *Clim. Dyn.*, *24*, 347–354, doi:10.1007/s00382-004-0505-y.

Locarnini, R. A., A. V. Mishonov, J. I. Antonov, T. P. Boyer, and H. E. Garcia (2006), *World Ocean Atlas 2005, vol. 1, Temperature, NOAA Atlas NESDIS 61*, U.S. Gov. Print. Off., Washington, D. C.

Lohmann, K., H. Drange, and M. Bentsen (2009), A possible mechanism for the strong weakening of the North Atlantic subpolar gyre in the mid-1990s, *Geophys. Res. Lett.*, *36*, L15602, doi:10.1029/2009GL039166.

Marshall, J., and F. Schott (1999), Open-ocean convection: Observations, theory and models, *Rev. Geophys.*, *37*, 1–64, doi:10.1029/98RG02739.

McCarthy, G., E. Frajka-Williams, W. E. Johns, M. O. Baringer, C. S. Meinen, H. L. Bryden, D. Rayner, A. Duchez, C. Roberts, and S. A. Cunningham (2012), Observed interannual variability of the Atlantic meridional overturning circulation at 26.5°N, *Geophys. Res. Lett.*, *39*, L19609, doi:10.1029/2012GL052933.

Meinen, C. S., A. R. Piola, R. C. Perez, and S. L. Garzoli (2012), Deep Western Boundary Current transport variability in the South Atlantic: Preliminary results from a pilot array at 34.5°S, *Ocean Sci. Discuss.*, *9*, 977–1008, doi:10.5194/osd-9-977-2012.

Meinen, C. S., S. Speich, R. C. Perez, S. Dong, A. R. Piola, S. L. Garzoli, M. O. Baringer, S. Gladyshev, and E. J. D. Campos (2013), Temporal variability of the meridional overturning circulation at 34.5°S: Results from two pilot boundary arrays in the South Atlantic, *J. Geophys. Res. Oceans*, *118*, 6461–6478, doi:10.1002/2013JC009228.

Mello, R. L., A. C. N. Freitas, L. Russo, J. F. Oliveira, C. A. S. Tanajura, and J. B. R. Alvarenga (2013), Ocean forecasts in the southwestern Atlantic: Impact of different sources of sea surface height in data assimilation, *Rev. Bras. Geofís.*, *31*(2), 243–255.

Mielke, C., E. Frajka-Williams, and J. Baehr (2013), Observed and simulated variability of the AMOC at 26°N and 41°N, *Geophys. Res. Lett.*, *40*, 1159–1164, doi:10.1002/grl.50233.

Montgomery, R. B. (1974), Comments on ''Seasonal variability of the Florida current'', by Niiler and Richardson, *J. Mar. Res.*, *32*, 533–535.

Park, J.-H., and D. R. Watts (2005), Response of the southwestern Japan/East Sea to the atmospheric pressure, *Deep Sea Res., Part II*, *52*, 1671–1683, doi:10.1016/j.dsr2.2003.08.007.

Perez, R. C., S. L. Garzoli, C. Meinen, and R. P. Matano (2011), Geostrophic velocity measurement techniques for the meridional overturning circulation and meridional heat transport in the South Atlantic, *J. Atmos. Oceanic Technol.*, *28*(11), 1504–1521, doi:10.1175/JTECH-D-11-00058.1.

Pond, S., and G. L. Pickard (1983), *Introductory Dynamical Oceanography*, 2nd ed., Pergamon Int. Lib. of Sci., Technol., Eng. and Social Stud. Elsevier Butterworth-Heinemann, Oxford, U. K.

Rahmstorf, S. (1996), On the freshwater forcing and transport of the Atlantic thermohaline circulation, *Clim. Dyn.*, *12*, 799–811, doi:10.1007/s003820050144.

Rayner, D., et al. (2011), Monitoring the Atlantic meridional overturning circulation, *Deep Sea Res., Part II*, *58*(17–18), 1744–1753, doi:10.1016/j.dsr2.2010.10.056.

 © 2014. American Geophysical Union. All Rights Reserved.

Richardson, P., and S. Garzoli (2003), Characteristics of intermediate water flow in the Benguela Current as measured with RAFOS floats, *Deep Sea Res., Part II*, *50*, 87–118, doi:10.1016/S0967-0645(02)00380-6.

Sabine, C., et al. (2004), The oceanic sink for anthropogenic CO_2, *Science*, *305*, 367–371, doi:10.1126/science.1097403.

Shriver, J. F., and H. E. Hurlburt (2000), The effect of upper ocean eddies on the non-steric contribution to the barotropic mode, *Geophys. Res. Lett.*, *27*, 2713–2716, doi:10.1029/1999GL011105.

Sime, L. C., D. P. Stevens, K. J. Heywood, and K. I. Oliver (2006), A decomposition of the Atlantic meridional overturning, *J. Phys. Oceanogr.*, *36*(12), 2253–2270, doi:10.1175/JPO2974.1.

Stramma, L., and M. England (1999), On the water masses and mean circulation of the South Atlantic Ocean, *J. Geophys. Res.*, *104*, 20,863–20,883, doi:10.1029/1999JC900139.

Sutton, R. T., and D. L. R. Hodson (2005), Atlantic Ocean forcing of North American and European summer climate, *Science*, *309*, 115–118, doi:10.1126/science.1109496.

Thacker, W. C. (2008), Estimating salinity between 25° and 45°S in the Atlantic ocean using local regression, *J. Atmos. Oceanic Technol.*, *25*, 114–130, doi:10.1175/2007JTECHO530.1.

Timmermann, A., et al. (2007), The influence of a weakening of the Atlantic meridional overturning circulation on ENSO, *J. Clim.*, *20*, 4899–4919, doi:10.1175/JCLI4283.1.

Treguier, A. M., M. England, S. R. Rintoul, G. Madec, J. L. Sommer, and J.-M. Molines (2007), Southern Ocean overturning across streamlines in an eddying simulation of the Antarctic circumpolar current, *Ocean Sci.*, *3*, 491–507, doi:10.5194/os-3-491-2007.

Wainer, I., P. Gent, and G. Goni (2000), Annual cycle of the Brazil-Malvinas confluence region in the National Center for Atmospheric Research climate system model, *J. Geophys. Res.*, *5*, 26,167–26,177, doi:10.1029/1999JC000134.

Weijer, W., W. P. M. D. Ruijter, H. A. Dijkstra, and P. J. van Leeuwen (1999), Impact of interbasin exchange on the Atlantic overturning circulation, *J. Phys. Oceanogr.*, *29*, 2266–2284.

Willis, J., and L.-L. Fu (2008), Combining altimeter and subsurface float data to estimate the time-averaged circulation in the upper ocean, *J. Geophys. Res.*, *113*, C12017, doi:10.1029/2007JC004690.

Woollings, T., J. M. Gregory, J. G. Pinto, M. Reyers, and D. J. Brayshaw (2012), Response of the North Atlantic storm track to climate change shaped by ocean-atmosphere coupling, *Nat. Geosci.*, *5*, 313–317, doi:10.1038/ngeo1438.

Xu, X., E. P. Chassignet, W. E. Johns, W. J. Schmitz Jr., and E. J. Metzger (2014), Intraseasonal to interannual variability of the Atlantic meridional overturning circulation from eddy-resolving simulations and observations, *J. Geophys. Res. Oceans*, *119*, 5140–5159, doi:10.1002/2014JC009994.

Zhang, R., and T. L. Delworth (2006), Impact of Atlantic multidecadal oscillations on India/Sahel rainfall and Atlantic hurricanes, *Geophys. Res. Lett.*, *33*, L17712, doi:10.1029/2006GL026267.

© 2014. American Geophysical Union. All Rights Reserved.